

Cascaded Composite Turbulence and Misalignment: Statistical Characterization and Applications to Reconfigurable Intelligent Surface-Empowered Wireless Systems

Alexandros-Apostolos A. Boulogeorgos, Senior Member, IEEE, Nestor Chatzidiamantis, Member, IEEE, Harilaos G. Sandalidis, Angeliki Alexiou, Member, IEEE, and Marco Di Renzo, Fellow, IEEE

Abstract—Reconfigurable intelligent surfaces (RISs) empowered high-frequency (HF) wireless systems are expected to become the supporting pillar for several reliability and data-rate hungry applications. Such systems are, however, sensitive to misalignment and atmospheric phenomena including turbulence. Most of the existing studies on the performance assessment of RIS-empowered wireless systems ignore the impact of the aforementioned phenomena. Motivated by this, the current contribution presents a theoretical framework for statistically characterizing cascaded composite turbulence and misalignment channels. More specifically, we present the probability density and cumulative distribution functions for the cascaded composite turbulence and misalignment channels. Building upon the derived analytical expressions and in order to demonstrate the applicability and importance of the extracted framework in different use case cases of interest, we present novel closed-form formulas that quantify the joint impact of turbulence and misalignment on the outage performance for two scenarios, namely cascaded multi-RIS-empowered free space optics (FSO) and terahertz (THz) wireless systems. For the aforementioned scenarios, the diversity order is extracted. In addition, we provide an insightful outage probability upper-bound for a third scenario that considers parallel multi-RIS-empowered FSO systems. Our results highlight the importance of accurately modeling both turbulence and misalignment when assessing the performance of such systems.

Index Terms—Optical wireless communications, outage probability, performance analysis, reconfigurable intelligent surfaces, statistical characterization, THz wireless communications.

I. INTRODUCTION

By envisioning unprecedented performance requirements in terms of data-rates, reliability, availability, and security, the sixth generation (6G) wireless era comes with the promise to become the pillar of several “killer-applications”, including

A.-A. A. Boulogeorgos and A. Alexiou are with the of Digital Systems, University of Piraeus Piraeus 18534 Greece (e-mails: al.boulogeorgos@ieee.org, alexiou@unipi.gr).

N. Chatzidiamantis is with the Department of Electrical and Computer Engineering, Aristotle University of Thessaloniki, 54124 Thessaloniki, (e-mail: nestoras@auth.gr).

H. G. Sandalidis is with the Department of Computer Science and Biomedical Informatics, University of Thessaly, 35131 Lamia, Greece, (e-mail: sandalidis@dib.uth.gr).

M. Di Renzo is with Université Paris-Saclay, CNRS, CentraleSupélec, Laboratoire des Signaux et Systèmes, 3 Rue Joliot-Curie, 91192 Gif-sur-Yvette, France. (marco.di-renzo@universite-paris-saclay.fr)

This work has received funding from the European Unions Horizon 2020 research and innovation programme under grant agreement No. 871464 (ARIADNE).

A part of this work was submitted to IEEE International Conference on Communications (ICC) 2021.

but not limited to extended reality, high-speed kiosks, and wireless backhauling [1]–[4]. To achieve these goals, two technology enablers are identified and expected to be exploited, namely high-frequency (HF) communications, in the sub-terahertz, terahertz (THz) [5]–[8] and optical bands [9]–[11], and reconfigurable intelligent surfaces (RISs) [12]–[15]. THz and optical wireless systems can support aggregated data rates that may exceed 1 Tb/s [5], [16]–[19]; thus, as envisioned, theoretically investigated and experimentally validated in [3], [20]–[30], they can be used as wireless fiber extenders. Indicatively, in [25], a 1 km wireless fiber extender was documented that operates at 300 GHz, while, in [26], a 500 m THz demonstrator was reported. In [29], a 100 m, FSO demonstrator was presented. In [30], finally, an 800 m outdoor point-to-point optical wireless link was demonstrated.

Despite the paramount importance that HF systems can play as wireless fiber extenders due to their sensitivity to blockages, they are unable to guarantee neither high-reliability nor continuous availability [31]–[34]. On the other hand, RISs are programmable metasurfaces, which are capable of altering the electromagnetic characteristics of the propagation medium, thus transforming conventional communication environments into smart platforms [12], [35]–[37]. In more detail, two of the most commonly examined RIS functionalities are blockage avoidance by creating alternative paths through beam-steering [38]–[40], which ensures uninterrupted connectivity between the source (S) and the final destination (D), and beam focusing in order to extend the system transmission distance [41], [42].

Motivated by these considerations, a great amount of effort has been very recently put on combining the aforementioned technologies and designing RISs that operate either in the THz or the optical band [43]–[49]. In [43] and [44], the authors presented a vanadium dioxide (VO_2)-based multi-functional RIS capable of manipulating THz waves, whereas a large-scale RIS that employs arrays of complementary metal-oxide-semiconductor (CMOS)-based chip tiles and operates at 0.3 THz was documented in [45]. In [46], a THz graphene plasmonic metasurface was reported, while a broadband non-linear plasmonic metasurface THz emitter operating in the THz band was demonstrated in [47]. Similarly, a graphene-based RIS structure that provides beam steering and focusing capabilities at frequencies around 4.35 THz was discussed

in [48]. In [49], a micro-electro-mechanical (MEM)-based THz RIS was demonstrated.

In addition, optical RISs have attracted a considerable attention [50]–[56]. In [50], a MEM was employed as an optical RIS in order to provide beam-steering capabilities in an optical wireless communication (OWC) system, while all-dielectric metasurfaces capable of manipulating near infrared waves were reported in [51]. The authors of [52] presented metalens-based metasurfaces that enable diffraction-limited focusing at wavelengths of 405, 532, and 660 nm, whereas an achromatic gallium nitride (GaN)-based optical RIS that operates in the entire visible region was reported in [53]. In [54], an optical RIS, which is capable of controlling the angular dispersions, enabling functionalities that range from perfect mirroring to angular multiplexing, was documented. In [55], in addition, two types of optical RISs were presented based on MEMs and phase array based technologies. Finally, in [56], an achromatic metasurface capable of eliminating the chromatic aberration over a continuous region from 1200 to 1680 nm for circularly-polarized incidence light in a reflection scheme was reported.

From the performance analysis, system design, and optimization points of view, the error performance of RIS-empowered THz wireless satellite systems in the presence of antenna misalignment were studied in [57]. In [58], the outage, error, and capacity performance of a single-RIS-empowered THz wireless system in the presence of $\alpha - \mu$ fading and antenna misalignment was analyzed. In [59], a capacity evaluation of RIS-empowered sub-THz wireless systems was conducted. In [60], the authors assessed the joint impact of hardware imperfections and antenna misalignment on RIS-empowered indoor THz wireless systems, whereas the coverage performance of RIS-empowered THz wireless systems were quantified in [61]. In [62], the authors introduced a multi-RIS-empowered THz hybrid beamforming architecture and formulated the design problem of the digital and analog beamforming matrices, assuming that all the intermediate channels, between the transmitter and the receiver, experience neither fading nor misalignment. In [63], in addition, a holographic RIS-empowered THz massive multiple-input multiple-output (MIMO) system accompanied by a low-overhead closed-loop channel estimation scheme was presented. In [64] the authors presented a sum-rate maximization framework for RIS-empowered THz wireless systems, by assuming that the transmitter-RIS and RIS-destination channels have a Rician distribution. In [65], the authors studied the problem of proactive handoff and beam selection in THz drone communication networks assisted with RIS. Similarly, in [66], the joint optimization problem of drone's trajectory, the phase shift of RIS, the allocation of THz sub-bands, and the power control were investigated aiming to maximize the minimum average achievable rate of all users. In [67], finally, a simultaneous terahertz (THz) information and power transfer system was introduced and the problem of maximizing the information users' data rate while ensuring the energy users' and RIS's power harvesting requirements was formulated and solved. It is worth mentioning that all the aforementioned works assume that the RISs have horizontal and vertical meta-atom

periodicity of the order of half of the wavelength.

The performance of RIS-empowered OWC systems was analyzed in [68]–[71]. In [68], the received signal-to-noise-ratio (SNR) in RIS-empowered visible light communication systems were evaluated. In [69], the authors studied the performance of a single-RIS-empowered OWC system in the presence of random obstacles and pointing errors, assuming that the impact of turbulence can be neglected. In [70], the authors considered a single-RIS free-space-optics (FSO) system and quantified its outage performance by devising an equivalent mirror-assisted FSO system that generates a reflected electric field on a mirror, which is identical to that on the source. Although this approach seems very promising, it cannot capture the statistics of the two cascaded links. Inspired by this, a closed-form expression for the outage probability (OP) of a single-RIS-empowered FSO system, in which both links experience different levels of turbulence and misalignment, was derived in [71].

Recently, the concept of using multiple-RISs to provide uninterrupted connectivity between pairs of transmitters and receivers was reported in [72]. Multi-RIS can enable a number of novel functionalities including, but not limited to blockage avoidance, routing, coverage expansion, and beam splitting. Despite the importance and capabilities that this concept can offer, to the best of the authors' knowledge, a theoretical framework for analyzing the achievable performance of such systems has not been formulated yet. This is due to the lack of a statistical model for the cascaded composite turbulence and misalignment fading channels. Motivated by this, in this paper, we introduce an analytical framework that covers the aforementioned gap as well as its applications in RIS-empowered wireless systems. In particular, the technical contribution of this work is as follows:

- We present closed-form expressions for the probability density function (PDF) and cumulative distribution function (CDF) for cascaded channels that experience different levels of turbulence.
- We derive a novel analytical expression for the PDF of cascaded channels that experience misalignment fading.
- Building upon the aforementioned expressions, we statistically characterize cascaded channels that experience different levels of turbulence and misalignment fading, in terms of PDF and CDF.
- We apply the obtained analytical frameworks for quantifying the outage performance of three relevant application scenarios, namely: i) a cascaded multi-RIS empowered FSO system, ii) a multi-RIS empowered FSO systems, and iii) a cascaded multi-RIS empowered THz wireless system. More precisely, in the first scenario, we introduce an accurate closed-form expression for the system OP that takes into account both the characteristics of the transmitter, receiver and propagation channel. For the second scenario, we report an OP upper-bound, and for the third scenario, we provide a closed-form expression for the OP that accounts for the impact of transceivers hardware imperfections.
- We provide the diversity order of the cascaded multi-RIS empowered FSO and THz systems.

The rest of this contribution is structured as follows: The statistical characterization of cascaded wireless channels that experience turbulence and/or misalignment fading is presented in Section II. Some applications of the analytical framework are discussed in Section III, while respective Monte Carlo simulations that verify the theoretical framework, accompanied by insightful discussions, are illustrated in Section IV. Finally, a summary of our main findings and concluding remarks are provided in Section V.

Notations: The absolute value, exponential and natural logarithm functions are respectively denoted by $|\cdot|$, $\exp(\cdot)$, and $\ln(\cdot)$. \sqrt{x} and $\prod_{l=1}^L x_l$ respectively return the square root of x , and the product of $x_1 x_2 \cdots x_L$. $\Pr(\mathcal{A})$ denotes the probability for the event \mathcal{A} to be valid. The modified Bessel function of the second kind of order n is denoted as $K_n(\cdot)$ [73, eq. (8.407/1)]. The Gamma [73, eq. (8.310)] function is denoted by $\Gamma(\cdot)$, and the error-function is represented by $\text{erf}(\cdot)$ [73, eq. (8.250/1)]. The generalized hypergeometric function is denoted by ${}_pF_q(a; b; z)$. Finally, $G_{p,q}^{m,n} \left(x \left| \begin{matrix} a_1, a_2, \dots, a_p \\ b_1, b_2, \dots, b_q \end{matrix} \right. \right)$ stands for the Meijer G-function [73, eq. (9.301)]. Tables I and II provide the definitions of all the symbols that are employed in this paper.

II. STATISTICAL CHARACTERIZATION OF PRODUCT CHANNELS

Let Z_1 be the product of $N \geq 1$ independently distributed Gamma-Gamma (GG) random variables (RVs), i.e.,

$$Z_1 = \prod_{i=1}^N r_i, \quad (1)$$

where r_i , with $i \in [1, N]$, is the i -th distributed GG RV. The PDF of r_i can be written as follows [74], [75]

$$f_{r_i}(x) = \frac{2}{\Gamma(\alpha_i) \Gamma(\beta_i)} \left(\frac{\alpha_i \beta_i}{\Omega_i} \right)^{\frac{\alpha_i + \beta_i}{2}} x^{\frac{\alpha_i + \beta_i}{2} - 1} \times K_{\alpha_i - \beta_i} \left(\alpha_i - \beta_i, 2\sqrt{\frac{\alpha_i \beta_i x}{\Omega_i}} \right), \quad (2)$$

where $\alpha_i \geq 0$ and $\beta_i \geq 0$ are the shaping parameters of the r_i distribution and Ω_i is the corresponding mean, i.e., $\Omega_i = \mathbb{E}_{r_i}[x]$. Of note, the distribution in (2) is generic, since, for different combinations of α_i and β_i , it returns various models that are usually used in communication systems. For $\alpha_i \rightarrow \infty$, it approximates the Gamma distribution, which have been widely used to model the fading of radio frequency systems. For $\alpha_i = 1$, it returns the K distribution that is suitable for wireless systems with strong line-of-sights components, such as in HF systems. For the special case of $\alpha_i = \beta_i = 1$, finally, it reduces to the PDF of the double Rayleigh distribution.

The following theorem provides closed-form expressions for the evaluation of the PDF and the CDF of Z_1 .

Theorem 1. *The PDF of Z_1 can be evaluated as*

$$f_{Z_1}(x) = \frac{G_{0,2N}^{2N,0} \left[x \prod_{i=1}^N \frac{\alpha_i \beta_i}{\Omega_i} \middle| \alpha_1, \beta_1, \alpha_2, \beta_2, \dots, \alpha_N, \beta_N \right]}{x \prod_{i=1}^N \Gamma(\alpha_i) \Gamma(\beta_i)}, \quad (3)$$

whereas, its CDF can be obtained as

TABLE I: Parameters and performance indicators definition.

Parameters	
p	Atmospheric pressure
T	Atmospheric temperature
P_s	Average power constraint of the FSO signal
B	Bandwidth
k_B	Boltzman's constant
A_Q	Derivative of the real-part of the refraction index with respect to the relative humidity
A_T	Derivative of the real-part of the refraction index with respect to the temperature
g_i	Deterministic path-gain coefficient of the i -th THz link
d_i	Distance of the i -th link
$g_{f,i}$	Free-space path-gain coefficient of the i -th THz link
$\tau(f, d)$	Molecular absorption gain coefficient
$\kappa(f)$	Molecular absorption coefficient
N	No. of Gamma-Gamma (GG) distributed random variables (RVs)
L	No. of misaligned links
f	Operation frequency
G_d	Reception antenna gain
ϕ	Relative humidity
p_w	Saturated water vapor partial pressure
C_T	Structure factor
G_s	Transmission antenna gain
s_i	Transmission signal of the i -th S at the parallel multi-RIS FSO
μ_w	Volume mixing ratio of the water vapor
η	Photodetector (PD) responsivity
c	Speed of light
λ	Wavelength of the optical carrier
α	Weather dependent attenuation coefficient
G_i	i -th FSO link atmospheric gain
R_i	i -th RIS reflection coefficient
ρ_i	i -th optical RIS reflection efficiency
s	Intensity of the FSO transmitted signal
x	Transmission signal at the RIS-empowered THz wireless system
ρ_s	Transmission SNR multiplied by the deterministic path-gain of the multi-RIS FSO system
r_{th}	SNR threshold at the multi-RIS FSO system
ρ_{th}	SNR threshold at the parallel multi-RIS FSO system
α_i, β_i	Shaping parameters of r_i
Ω_i	Mean of r_i
$\xi_i, A_{o,i}$	Distribution parameters of l_i
σ_n^2	Variance of the additive white Gaussian shot noise
C_n^2	Refraction index parameters
$\sigma_{R_i}^2$	Rytov variance of the i -th FSO link
b_i	Radius of the circular aperture at the i -th RIS or D plane
w_{d_i}	Beam waste at the i -th RIS or D plane
$w_{\text{eq},i}$	Equivalent beam radius at the i -th RIS or D plane
$\sigma_{s,i}^2$	Pointing error displacement (jitter) variance
N_o	Noise variance
σ_s^2	Variance of η_s
σ_d^2	Variance of η_d
κ_s	Error vector magnitude of the S transmitter
κ_r	Error vector magnitude of the D receiver
Performance indicators	
P_o^{FSO}	Multi-RIS FSO system OP
P_o^{par}	Parallel multi-RIS FSO system OP
P_o^{THz}	RIS-empowered THz wireless system OP

$$F_{Z_1}(x) = \frac{1}{\prod_{i=1}^N \Gamma(\alpha_i) \Gamma(\beta_i)} \times G_{1,2N+1}^{2N,1} \left[x \prod_{i=1}^N \frac{\alpha_i \beta_i}{\Omega_i} \middle| \alpha_1, \beta_1, \alpha_2, \beta_2, \dots, \alpha_N, \beta_N, 0 \right]. \quad (4)$$

Proof: The product of gamma-gamma RVs is a special case of the product of generalized-gamma RVs derived in [76, eqs. (2) and (9)]. By setting the suitable parameter in [76, eqs. (2) and (9)] and after some algebraic manipulations, we

TABLE II: Random variables (RVs) definition.

r_i	i -th GG distributed RV
l_i	Misalignment fading coefficient of the i -th misaligned link
Z_1	Product of independent distributed GG RVs
Z_2	Product of $l_i, i = 1, \dots, L$ RVs
A	Cascaded multi-RIS empowered FSO end-to-end (e2e) channel
h_i	Turbulence coefficient of the i -th FSO link
$h_{p,i}$	Misalignment fading coefficient of the i -th FSO link
B_i	E2e channel coefficient of the i -th FSO link
$h_{1,i}$	i -th S -RIS link turbulence coefficient
$h_{2,i}$	i -th RIS- D link turbulence coefficient
$h_{p1,i}$	i -th S -RIS link misalignment fading coefficient
$h_{p2,i}$	i -th RIS- D link misalignment fading coefficient
n	Additive white Gaussian shot noise
A_t	THz e2e channel coefficient
$h_{p,i}^{\text{THz}}$	Misalignment fading coefficient of the i -th THz link
$h_{t,i}^{\text{THz}}$	Turbulence coefficient of the i -th THz link
w	AWGN at the D of the RIS-empowered THz wireless system
r	Received signal at the multi-RIS FSO system
r_p	Received signal at the parallel multi-RIS FSO system
r_s	S distortion noise at the RIS-empowered THz wireless system
r_d	D distortion noise at the RIS-empowered THz wireless system
y	Received signal at D at the RIS-empowered THz wireless system
ρ_{FSO}	Instantaneous SNR at D of the multi-RIS FSO system
ρ_{par}	Instantaneous SNR at D of the parallel multi-RIS FSO system
γ	Signal-to-distortion-plus-noise-ratio (SDNR)

extract (3) and (4). This concludes the proof. ■

Let Z_2 be the product of $L, L \geq 1$, independent RVs, i.e.,

$$Z_2 = \prod_{i=1}^L l_i, \quad (5)$$

where l_i is the i -th RV and its PDF can be expressed as

$$f_{l_i}(x) = \frac{\xi_i}{A_{o,i}^{\xi_i}} x^{\xi_i-1}, \text{ with } 0 \leq x \leq A_{o,i}, \quad (6)$$

with ξ_i and $A_{o,i}$ being the distribution parameters of l_i . The following theorem provides a closed-form expression for the PDF of Z_2 .

Theorem 2. *The PDF of Z_2 can be expressed as*

$$f_{Z_2}(x) = \frac{1}{(L-1)!} \frac{\prod_{i=1}^L \xi_i}{\prod_{i=1}^L A_{o,i}^{\xi_i}} x^{\xi_L-1} \times \left(\ln \left(\frac{\prod_{i=1}^L A_{o,i}}{x} \right) \right)^{L-1} \quad (7)$$

with $0 \leq x \leq \prod_{i=1}^L A_{o,i}$.

Proof: For brevity, the proof of Theorem 2 is given in Appendix B. ■

For the special case in which $A_{o,1} = A_{o,2} = \dots = A_{o,M} = A_o$ and $\xi_1 = \xi_2 = \dots = \xi_M = \xi$, (7) can be simplified to

$$f_{Z_2}^{\text{sc}}(x) = \frac{1}{(L-1)!} \left(\frac{\xi}{A_o^\xi} \right)^L x^{\xi-1} \left(\ln \left(\frac{A_o^L}{x} \right) \right)^{L-1}, \quad (8)$$

with $0 \leq x \leq A_o^L$.

Theorem 3. *The PDF and CDF of*

$$Z = Z_1 Z_2, \quad (9)$$

can be formulated as shown in (10) and (11), given at the top of the next page.

Proof: For brevity, the proof of Theorem 3 is given in Appendix C. ■

It should be noted that the expressions of (10) and (11) can

be written in terms of more familiar hypergeometric functions according to [73, Eq. (9.303)]. In more detail, for the special, but very realistic, case in which no two elements of the tuple $\mathcal{B} = [\alpha_1, \dots, \alpha_N, \beta_1, \dots, \beta_N, \xi_1, \dots, \xi_L, 0]$ differ by an integer, (11) can be rewritten as in (12), given at the top of the next page. In (12), \mathcal{A}_i with $i = 1, \dots, L+1$ refers to the i -th element of the tuple $\mathcal{A} = \{1, \xi_1 + 1, \dots, \xi_L + 1\}$. Similarly, \mathcal{B}_i with $i = 1, \dots, 2N+L$ refers to the i -th of \mathcal{B} . According to [77]–[79], since Meijer-G can be expressed as a finite sum of hypergeometric functions, it is considered a closed-form expression. Moreover, notice that nowadays, the Meijer-G function can be directly computed in several software packages and programming languages, including, but not limited to, Mathematica, Maple, Matlab, Python, C++.

The following lemma return the limit of the CDF of Z as $x \rightarrow 0$.

Lemma 1. *In the case in which no two elements of the tuple \mathcal{B} differ by an integer, as x tends to 0, the limit of the CDF of Z can be approximated as*

$$F_Z^0(x) = \frac{\prod_{i=1}^L \xi_i}{\prod_{i=1}^N \Gamma(\alpha_i) \Gamma(\beta_i)} \times \sum_{i=1}^{2N+L} \frac{\prod_{j=1}^{2N+L} \Gamma(\mathcal{B}_j - \mathcal{B}_i) \Gamma(\mathcal{A}_i)}{\prod_{j=2N+L}^{2N+L+1} \Gamma(1 + \mathcal{B}_i - \mathcal{B}_j) \prod_{j=2}^{L+1} \Gamma(\mathcal{A}_j - \mathcal{B}_i)} x^{\mathcal{B}_i} \quad (13)$$

Proof: As $x \rightarrow 0$,

$${}_{L+1}F_{2N+L}(1 + \mathcal{B}_i - \mathcal{A}_1, \dots, 1 + \mathcal{B}_i - \mathcal{A}_{L+1}; 1 + \mathcal{B}_i - \mathcal{B}_1, \dots, 1 + \mathcal{B}_i - \mathcal{B}_{2N+L+1}; (-1)^{-2N} x) \rightarrow 1 \quad (14)$$

By applying (14) into (12), we obtain (13). This concludes the proof. ■

III. APPLICATIONS

This section is focused on presenting some applications of the theoretical framework. In more detail, three scenarios are considered: i) cascaded multi-RIS empowered FSO; ii) parallel multi-RIS empowered FSO; and iii) cascaded multi-RIS empowered wireless THz systems. For each scenario, the corresponding systems models are first presented and then closed-form expressions or upper bounds for the OP are computed.

A. Cascaded multi-RIS empowered FSO systems

1) *System model:* As depicted in Fig. 1, an FSO system, which comprises a source S equipped with a light source (LS), $N-1$ optical RISs, and a destination D equipped with a lens and a photo-detector (PD), is considered. The LS transmits a Gaussian beam towards the RIS. The i -th RIS reflects the incident beam towards the $(i+1)$ -th RIS until the $(N-1)$ -th RIS. The $(N-1)$ -th RIS reflects the incident beam towards the lens D , which focuses it to the PD. Of note, as reported in [55], the RIS is capable of changing the beam shape. We assume that the LS, RISs, and PD are located in fixed positions and that the i -th RIS shapes the beam in an optimal manner, i.e. in a way that its footprint at the $i+1$ -th RIS and the PD planes are a circle. Finally, it is assumed that the direct $S-D$ link is blocked, while all the intermediate RIS-empowered and RIS- D links are in line-of-sight (LoS).

The turbulence coefficient of the i -th link is represented by h_i , which can be modeled as a GG RV. Each link may or

$$f_Z(x) = \frac{\prod_{i=1}^L \xi_i}{\prod_{i=1}^N \Gamma(\alpha_i) \Gamma(\beta_i)} x^{-1} G_{L,2N+L}^{2N+L,0} \left(\frac{1}{\prod_{i=1}^N \frac{\Omega_i}{\alpha_i \beta_i} \prod_{i=1}^L A_{o,i}} x \mid \begin{matrix} 1 + \xi_1, 1 + \xi_2, \dots, 1 + \xi_L \\ \alpha_1, \dots, \alpha_N, \beta_1, \dots, \beta_N, \xi_1, \dots, \xi_L \end{matrix} \right) \quad (10)$$

$$F_Z(x) = \frac{\prod_{i=1}^L \xi_i}{\prod_{i=1}^N \Gamma(\alpha_i) \Gamma(\beta_i)} G_{L+1,2N+L+1}^{2N+L,1} \left(\frac{1}{\prod_{i=1}^N \frac{\Omega_i}{\alpha_i \beta_i} \prod_{i=1}^L A_{o,i}} x \mid \begin{matrix} 1, \xi_1 + 1, \dots, \xi_L + 1 \\ \alpha_1, \dots, \alpha_N, \beta_1, \dots, \beta_N, \xi_1, \dots, \xi_L, 0 \end{matrix} \right) \quad (11)$$

$$F_Z(x) = \frac{\prod_{i=1}^L \xi_i}{\prod_{i=1}^N \Gamma(\alpha_i) \Gamma(\beta_i)} \sum_{i=1}^{2N+L} \frac{\prod_{j=1}^{2N+L} \Gamma(\mathcal{B}_j - \mathcal{B}_i) \Gamma(\mathcal{A}_i)}{\prod_{j=2N+L}^{2N+L+1} \Gamma(1 + \mathcal{B}_i - \mathcal{B}_j) \prod_{j=2}^{L+1} \Gamma(\mathcal{A}_j - \mathcal{B}_i)} x^{\mathcal{B}_i} \\ \times {}_{L+1}F_{2N+L}(1 + \mathcal{B}_i - \mathcal{A}_1, \dots, 1 + \mathcal{B}_i - \mathcal{A}_{L+1}; 1 + \mathcal{B}_i - \mathcal{B}_1, \dots, 1 + \mathcal{B}_i - \mathcal{B}_{2N+L+1}; (-1)^{-2N} x) \quad (12)$$

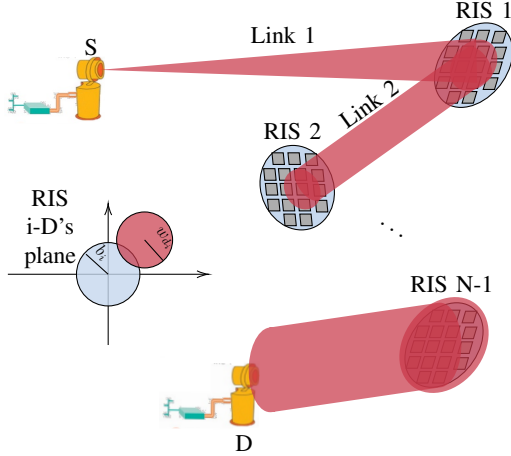


Fig. 1: Cascaded multi-RIS empowered FSO system model.

may not experience misalignment fading. Let us assume that L out of N links suffer from misalignment fading and let us model its impact on the i -th link through a coefficient $h_{p,i}$. Thus, the received signal at the PD of D can be written as

$$r = As + n, \quad (15)$$

where $s \in \mathbb{R}^+$ represents the intensity of the transmitted signal with $\mathbb{E}[s] \leq P$ with P being the average power constraint, $n \in \mathbf{R}$ stands for the additive white Gaussian shot noise with variance σ_n^2 , which is caused by the ambient light at the PD, and $A \in \mathbb{R}^+$ is the end-to-end (e2e) channel. The e2e channel coefficient can be expressed as

$$A = \eta \prod_{i=1}^L h_{p,i} h_i G_i \prod_{i=L+1}^N h_i G_i, \quad (16)$$

where η represents the PD responsivity, while G_i stands for the i -th link atmospheric gain and can be written as

$$G_i = \rho 10^{-\alpha(d_{i-1} + d_i)/10}. \quad (17)$$

In (17), ρ is the i -th RIS reflection efficiency that typically ranges in $[0.7, 1]$ [80], [81], α is a weather-dependent attenuation coefficient, d_{i-1} and d_i are the distances between the $i-1$ and i links, respectively. Furthermore, the parameters h_i follow the GG distribution with atmospheric parameters α_i and β_i , calculated based on d_{i-1} or d_{i+1} , the refraction index parameter C_n^2 and the wavelength of the optical carrier λ [82] according to the following formulas

$$\alpha_i = \left(\exp \left\{ \frac{0.49 \sigma_{R_i}^2}{\left(1 + 1.11 \sigma_{R_i}^{\frac{12}{5}}\right)^{\frac{7}{6}}} \right\} - 1 \right)^{-1} \quad (18)$$

and

$$\beta_i = \left(\exp \left\{ \frac{0.51 \sigma_{R_i}^2}{\left(1 + 0.69 \sigma_{R_i}^{\frac{12}{5}}\right)^{\frac{7}{6}}} \right\} - 1 \right)^{-1}. \quad (19)$$

Moreover, $\sigma_{R_i}^2$ is the Rytov variance given by

$$\sigma_{R_i}^2 = 1.23 C_n^2 \left(\frac{2\pi}{\lambda} \right)^{\frac{7}{6}} d_i^{\frac{11}{6}}, \quad (20)$$

with C_n^2 being the refractive index structure parameter, which is used to characterize the atmospheric turbulence.

Finally, the PDF $h_{p,i}$ can be obtained as in (6). In this scenario,

$$A_{o,i} = [\text{erf}(v_i)]^2 \quad (21)$$

stands for the fraction of the collected power in the ideal case of zero radial displacement. Moreover,

$$v_i = \frac{\sqrt{\pi} b_i}{\sqrt{2} w_{d_i}}. \quad (22)$$

with b_i and w_{d_i} representing the radius of the circular aperture at the i -th RIS, with $i \in [1, N-1]$, or D 's side, for $i = N$, respectively and the beam waste on the corresponding plane. Likewise, ξ_i is the equivalent beam radius, $w_{\text{eq},i}$, to the pointing error displacement standard deviation square ratio and can be calculated as

$$\xi_i = \frac{w_{\text{eq},i}^2}{4\sigma_{s,i}^2} \quad (23)$$

with $\sigma_{s,i}^2$ denoting the pointing error displacement (jitter) variance. Finally,

$$w_{\text{eq},i}^2 = w_{d_i}^2 \frac{\sqrt{\pi} \text{erf}(v_i)}{2v_i \exp(-v_i^2)}. \quad (24)$$

2) *Performance assessment*: The SNR at the RX can be expressed as

$$\rho_{\text{FSO}} = A^2 \rho_s, \quad (25)$$

where ρ_s stands for the transmission SNR multiplied by the deterministic path-gain. Thus, the OP is defined as

$$P_o^{\text{FSO}} = \Pr(\rho_{\text{FSO}} \leq r_{\text{th}}), \quad (26)$$

or, from (25),

$$P_o^{\text{FSO}} = \Pr\left(A \leq \sqrt{\frac{r_{\text{th}}}{\rho_s}}\right), \quad (27)$$

which, by applying (11), can be written in a closed-form expression. For the special case, in which $d_1 \neq d_2 \neq \dots \neq d_N$, (12) can be employed in order to assess the OP of the cascaded multi-RIS empowered FSO system. Of note, for the special case in which $N = L = 2$, $d_1 = d_2$, $b_1 = b_2$,

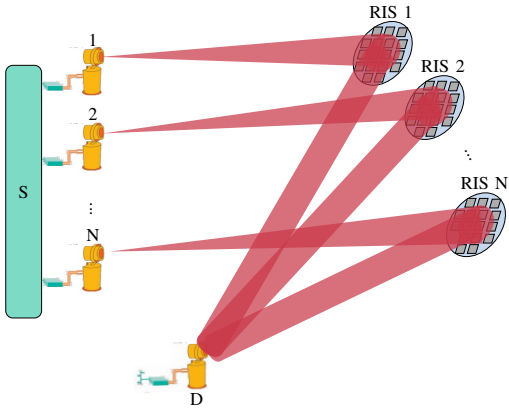


Fig. 2: Parallel Multi-RIS FSO system model.

$w_{d_1} = w_{d_2}$ and $\sigma_{s,1} = \sigma_{s,2}$, (27) can be written as in [71, eq. (15)].

The following lemma returns the diversity order of the cascaded multi-RIS empowered FSO system.

Lemma 2. *The diversity order of the cascaded multi-RIS empowered FSO system can be obtained as*

$$D_{FSO} = \min_{i=1, \dots, 2N+L} \mathcal{B}_i/2. \quad (28)$$

Proof: For $\rho_s \rightarrow \infty$, the term $\frac{r_{th}}{\rho_s}$ tend to 0; thus, based on (13), the outage probability can be approximated as

$$P_{o,\infty}^{FSO} = \frac{\prod_{i=1}^L \xi_i}{\prod_{i=1}^N \Gamma(\alpha_i) \Gamma(\beta_i)} \times \sum_{i=1}^{2N+L} \frac{\prod_{j=1}^{2N+L} \Gamma(\mathcal{B}_j - \mathcal{B}_i) \Gamma(\mathcal{A}_i)}{\prod_{j=2N+L}^{2N+L+1} \Gamma(1 + \mathcal{B}_i - \mathcal{B}_j) \prod_{j=2}^{L+1} \Gamma(\mathcal{A}_j - \mathcal{B}_i)} \times \left(\frac{r_{th}}{\rho_s} \right)^{\mathcal{B}_i/2}. \quad (29)$$

It is evident that in (29), $\left(\frac{r_{th}}{\rho_s} \right)^{\mathcal{B}_i/2}$ contributes with diversity order $\mathcal{B}_i/2$ in the asymptotic OP. Hence, the diversity order can be obtained as in (28). This concludes the proof. ■

B. Parallel Multi-RIS FSO systems

1) *System model:* As presented in Fig. 2, we consider a multi-RIS FSO system that consists of a S , N RIS, and a D . The S is equipped with N transmit apertures, each one at a different RIS. The i -th RIS steers the incident beam towards D , which is equipped with a single PD. Thus, the received signal at the destination can be expressed as

$$r_p = \sum_{i=1}^N \mathcal{B}_i s_i + n, \quad (30)$$

where s_i is the transmission signal by the i -th S 's aperture, while

$$\mathcal{B}_i = h_{p_{1,i}} h_{p_{2,i}} h_{1,i} h_{2,i} G_i, \quad (31)$$

represents the S - i -th RIS- D channel coefficient. In more detail, in (31), $h_{p_{1,i}}$ and $h_{p_{2,i}}$ denote the fading misalignment coefficient of the S - i -th RIS and i -th RIS- D links, respectively, whereas $h_{1,i}$ and $h_{2,i}$ are the turbulence coefficients of the S - i -th RIS and i -th RIS- D links, respectively.

2) *Performance assessment:* By assuming that the total transmission power, P_s , is equally divided into the N transmis-

sion apertures, the instantaneous SNR at D can be obtained as

$$\rho_{par} = \frac{\left(\sum_{i=1}^N \mathcal{B}_i \right)^2 P_s}{N N_o}, \quad (32)$$

or equivalent

$$\rho_{par} = N S^2 \rho_s, \quad (33)$$

where

$$S = \frac{1}{N} \sum_{i=1}^N \mathcal{B}_i. \quad (34)$$

From (33), the OP can be expressed as

$$P_o^{par} = \Pr(\rho_{par} \leq \rho_{th}), \quad (35)$$

or equivalently

$$P_o^{par} = \Pr\left(S \leq \sqrt{\frac{\rho_{th}}{N \rho_s}}\right), \quad (36)$$

or

$$P_o^{par} = F_S\left(\sqrt{\frac{\rho_{th}}{N \rho_s}}\right), \quad (37)$$

with $F_S(\cdot)$ being the CDF of S . According to [83, eq.(14)], the OP of the parallel multi-RIS FSO scenario can be upper bounded as

$$P_o^{par} \leq F_A\left(\left(\sqrt{\frac{\rho_{th}}{N \rho_s}}\right)^N\right). \quad (38)$$

C. RIS-empowered THz wireless systems

In this section, the system model and theoretical framework that quantifies the outage performance of multi-RIS-empowered outdoor THz wireless systems is provided. Note that this analysis can be also and straightforwardly extended to millimeter wave systems by replacing the term that describes the deterministic path-gain of the THz system with the corresponding one for the millimeter wave system.

1) *System model:* A multi-RIS-empowered outdoor THz wireless systems is considered, in which S and D are equipped with high-directional antennas. This system can be used a wireless fiber extender; thus, both the S and D antennas are placed high, e.g., in rooftops. Again, it is assumed that due to static obstacles, e.g., buildings¹, no direct link between the S and D can be established; as a result, N RISs are used. Each RIS can be seen as a reflector that steers and/or focuses the beams towards the desired direction. Thus, the received signal at D can be obtained as

$$y = A_t(x + \eta_s) + \eta_d + w, \quad (39)$$

where x is the transmission signal, while w stands for the AWGN. Moreover, η_s and η_d are the S and D distortion noises, due to transmitter's and receiver's hardware imperfections, respectively. According to [84]–[87], η_s and η_d can be modeled as two independent RVs that, for a given channel realization, have zero-mean complex Gaussian distributions with variances

$$\sigma_s^2 = \kappa_s^2 P_s \text{ and } \sigma_d^2 = \kappa_r^2 A^2 P_s, \quad (40)$$

respectively. In (40), κ_t and κ_r stand for the error vector magnitude of the S 's transmitter and the D 's receiver, while P_s denotes the transmission power.

Meanwhile, in (39), A_t represents the e2e channel, which

¹Note that, since the transmission and reception antennas as well as the RISs are placed high, no dynamic blockage is expected.

can be expressed as

$$A_t = \prod_{i=1}^L h_{p,i}^{\text{THz}} h_{t,i}^{\text{THz}} g_i \prod_{i=L+1}^N h_{t,i}^{\text{THz}} g_i. \quad (41)$$

In (41), $h_{p,i}^{\text{THz}}$ and $h_{t,i}^{\text{THz}}$ are the misalignment fading and turbulence coefficients that are distributed according to (6) and (2), respectively. Note that the turbulence model that is employed has been experimentally validated in [88], theoretically analyzed in [89], and supported by ITU-R [90]. The α_i and β_i parameters of (2) can be evaluated according to [89] as

$$\alpha_i^{\text{THz}} = \left(\exp \left(\frac{0.49\sigma_{R_i}^2}{(1 + 0.65D_i^2 + 1.11\sigma_{R_i}^{12/5})^{7/6}} \right) - 1 \right)^{-1} \quad (42)$$

and

$$\beta_i^{\text{THz}} = \left(\exp \left(\frac{0.51\sigma_{R_i}^2 (1 + 0.69\sigma_{R_i}^{12/5})^{-5/6}}{1 + 0.9D_i^2 + 0.62D_i^2\sigma_{R_i}^{12/5}} \right) - 1 \right)^{-1} \quad (43)$$

while $\sigma_{R_i}^2$ can be obtained as in (20). Additionally,

$$D_i = \sqrt{\frac{\pi b_i^2}{2\lambda d_i}}. \quad (44)$$

According to ITU-T, in the THz band, the reflection index structure parameter can be formulated as [91]

$$C_n^2 = \frac{C_T^2}{T} (A_T^2(\lambda) + 10^4 A_Q^2(\lambda) \pm 200 A_T(\lambda) A_Q(\lambda)), \quad (45)$$

where T stands for the temperature, C_T denotes the structure factor for the temperature, while A_T and A_R are the derivatives of the real part of the refractive index with respect to the temperature and humidity, respectively. Finally, g_i represents the deterministic path-gain coefficient of the i -th link and can be written as

$$g_i = g_{f,i}(f, d_i) \tau(f, d_i), \quad (46)$$

where $g_{f,i}$ denotes the free space path loss coefficient, which based on the Friis transmission equation, can be expressed as

$$g_{f,i}(f, d_i) = \begin{cases} \frac{c}{4\pi f d_i} \sqrt{G_s}, & \text{for } i = 1 \\ \frac{c}{4\pi f d_i} R_{i-1}, & \text{for } i \in [2, N-1] \\ \frac{c}{4\pi f d_i} \sqrt{G_d}, & \text{for } i = N \end{cases}, \quad (47)$$

whereas $\tau(f, d_i)$ denotes the molecular absorption coefficient and can be obtained as

$$\tau(f, d_i) = \exp \left(-\frac{1}{2} \kappa(f) d_i \right). \quad (48)$$

In (47), f and c stand for the transmission frequency and the speed of light, respectively, while G_s , R_i and G_d represent the S transmission antenna gain, the i -th RIS reflection coefficient, and the D reception antenna gain, respectively. Likewise, in (48), $\kappa(f)$ denotes the molecular absorption coefficient, which depends on the atmospheric temperature (T), pressure (p), as well as relative humidity (ϕ) and can be evaluated as in [92], [93] and [94, eq. (8)]

$$\kappa(f) = g(f) + g_1 + g_2, \quad (49)$$

where

$$g(f) = \sum_{i=0}^3 p_i f^i, \quad (50)$$

with $p_0 = -6.36$, $p_1 = 9.06$, $p_2 = -3.94$ and $p_3 = 5.54$.

Moreover,

$$g_1 = \frac{G_A(\mu_w)}{G_B(\mu_w) + \left(\frac{f}{100c} - c_0 \right)^2}, \quad (51)$$

where $G_A(\mu_w) = 0.2205\mu_w(0.1303\mu_w + 0.0294)$, $G_B(\mu_w) = (0.4093\mu_w + 0.0925)^2$, $c_0 = 10.835$ with μ_w being the volume mixing ratio of the water vapor and can be computed as

$$\mu_w = \frac{\phi}{100} \frac{p_w(T, p)}{p}. \quad (52)$$

In (52), $p_w(T, p)$ is the saturated water vapor partial pressure and can be expressed as

$$p_w(T, p) = k_1 (k_2 + k_3 \phi_p) \exp \left(\frac{k_4 (T - T_1)}{T - T_2} \right), \quad (53)$$

where $k_1 = 6.1121$, $k_2 = 1.0007$, $k_3 = 3.46 \times 10^{-6}$ hPa $^{-1}$, $k_4 = 17.502$, $T_1 = 273.15^\circ\text{K}$, and $T_2 = 32.18^\circ\text{K}$. Finally,

$$g_2 = \frac{G_C(\mu_w)}{G_D(\mu_w) + \left(\frac{f}{100c} - c_1 \right)^2}, \quad (54)$$

where $G_C(\mu_w) = 2.014\mu_w(0.1702\mu_w + 0.0303)$, $G_D = (0.537\mu_w + 0.0956)^2$ and $c_1 = 12.664$.

2) *Performance assessment*: From (39), the signal-to-distortion-plus-noise-ratio (SDNR) can be obtained as

$$\gamma = \frac{A_t^2 P_s}{A_t^2 (\kappa_t^2 + \kappa_r^2) P_s + N_o}, \quad (55)$$

where N_o is the noise variance. Moreover, the OP is defined as

$$P_o^{\text{THz}} = \Pr(\gamma < \gamma_{\text{th}}), \quad (56)$$

where γ_{th} represents the SNR threshold. With the aid of (55), (56) can be rewritten as

$$P_o^{\text{THz}} = \begin{cases} \Pr \left(A_t^2 \leq \frac{1}{1 - \gamma_{\text{th}} (\kappa_t^2 + \kappa_r^2)} \frac{\gamma_{\text{th}}}{\gamma_s} \right), & \text{for } \gamma_{\text{th}} \leq \frac{1}{\kappa_t^2 + \kappa_r^2} \\ 1, & \text{for } \gamma_{\text{th}} > \frac{1}{\kappa_t^2 + \kappa_r^2} \end{cases}. \quad (57)$$

Finally, by applying (41) in (57), we get (58), given at the top of the next page. In (58), γ_s is the transmission SNR multiplied by the deterministic path-gain, i.e.,

$$\gamma_s = \frac{P_s \prod_{i=1}^N g_i}{N_o}. \quad (59)$$

Note that from (58), it becomes evident that hardware imperfections set a limit to the maximum allowed spectral efficiency of the transmission scheme. In more detail, since the spectral efficiency, p , is connected with the SNR threshold through $p = \log_2(1 + \gamma_{\text{th}})$, choosing a p greater than $\log_2\left(1 + \frac{1}{\kappa_t^2 + \kappa_r^2}\right)$ would lead to an OP equal to 1.

The following lemma returns the diversity order of the multi-RIS empowered THz system.

Lemma 3. *The diversity order of the multi-RIS empowered THz system can be obtained as*

$$D_{\text{THz}} = \min_{i=1, \dots, 2N+L} \mathcal{B}_i^{\text{THz}} / 2, \quad (60)$$

where $\mathcal{B}_i^{\text{THz}}$ is the i -th element of the tuple

$$\mathcal{B}^{\text{THz}} = [\alpha_1^{\text{THz}}, \dots, \alpha_N^{\text{THz}}, \beta_1^{\text{THz}}, \dots, \beta_N^{\text{THz}}, \xi_1, \dots, \xi_L, 0] \quad (61)$$

Proof: This lemma can be proven by following the same steps as the proof of Lemma 2. ■

IV. RESULTS & DISCUSSION

This section focuses on verifying the theoretical framework presented in Section II by means of Monte Carlo simulations. To this end, lines are used to denote analytical results, while

$$P_o^{\text{THz}} = \begin{cases} F_Z \left(\sqrt{\frac{1}{1-\gamma_{\text{th}}(\kappa_t^2 + \kappa_r^2)} \frac{\gamma_{\text{th}}}{\gamma_s}} \right), & \text{for } \gamma_{\text{th}} \leq \frac{1}{\kappa_t^2 + \kappa_r^2} \\ 1, & \text{for } \gamma_{\text{th}} > \frac{1}{\kappa_t^2 + \kappa_r^2} \end{cases} \quad (58)$$

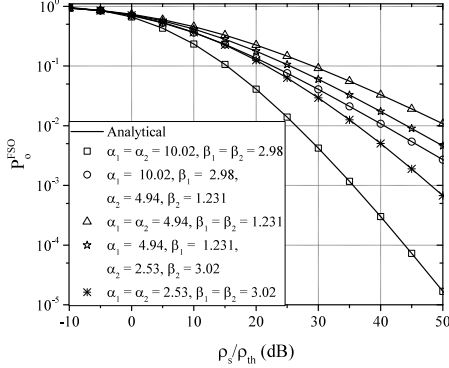


Fig. 3: OP vs ρ_s/ρ_{th} , for different levels of turbulence, assuming $N = 2$ and $L = 0$.

markers are employed for simulations. The rest of this section is organized as Section IV-A focuses on presenting numerical results that quantify the outage performance of cascaded multi-RIS-empowered FSO systems, whereas Section IV-B verifies the outage performance bounds of parallel multi-RIS-empowered FSO systems. Finally, in Section IV-C, the outage performance of cascaded multi-RIS-empowered THz wireless systems is assessed.

A. Cascaded multi-RIS-empowered FSO systems

Figure 3 quantifies the impact of turbulence in a multi-RIS-empowered FSO system, where $N = 2$ and $L = 0$. In more detail, the OP is plotted against ρ_s/ρ_{th} for different levels of turbulence. The following scenarios are considered: i) both the S -RIS and RIS- D links experience weak turbulence, i.e., $\alpha_1 = \alpha_2 = 10.02$ and $\beta_1 = \beta_2 = 2.98$, ii) either the S -RIS or the RIS- D link experience weak ($\alpha_1 = 10.02$ and $\beta_1 = 2.98$), while the other suffers from strong turbulence ($\alpha_2 = 4.942$ and $\beta_1 = 1.231$), iii) both links experience strong turbulence, iv) one link suffers from strong, while the other from moderate ($\alpha_2 = 2.53$ and $\beta_1 = 3.02$) turbulence and v) both links experience from moderate turbulence. This figure reveals that for fixed turbulence conditions, the RIS-empowered FSO system outage performance improves, as ρ_s/ρ_{th} increases. For example, for $\alpha_1 = \alpha_2 = 10.02$ and $\beta_1 = \beta_2 = 2.98$, as ρ_s/ρ_{th} changes from 25 to 35 dB, the OP decreases by about 10 times. Additionally, we observe that, for a fixed ρ_s/ρ_{th} , as the intensity of turbulence increases in either one of the S -RIS and RIS- D links, the outage performance degrades. For instance, for $\rho_s/\rho_{\text{th}} = 35$ dB, the OP increases for more than an order of magnitude as turbulence conditions changes from scenario i to ii. Interestingly, for a fixed ρ_s/ρ_{th} , the systems in which both links suffer from moderate turbulence may outperform the ones in which one link suffers from weak and the other from strong turbulence. This highlights the importance of accurately characterizing turbulence intensity when assessing the performance of RIS-empowered FSO systems.

Figure 4 assesses the impact of turbulence in FSO systems that employ multiple RISs. In particular, the OP is

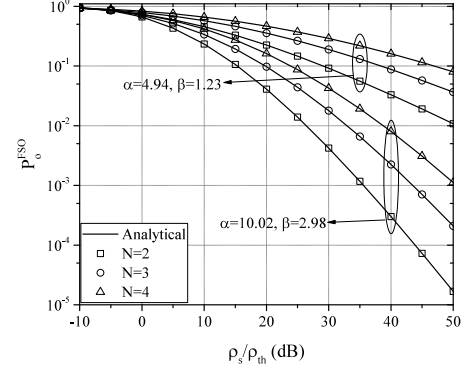


Fig. 4: OP vs ρ_s/ρ_{th} , for different values of N and levels of turbulence, assuming $L = 0$.

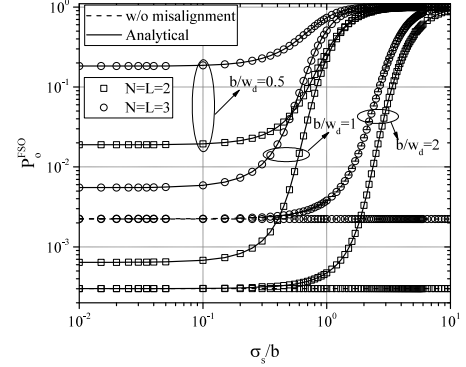


Fig. 5: OP vs σ_s/b , for different values of β/w_d and $N = L$.

depicted as a function of ρ_s/ρ_{th} , for different values of N and turbulence, assuming $L = 0$. For the turbulence intensity, the following two scenarios are considered: i) the best-case scenario, in which all the links suffer from weak turbulence, i.e., $\alpha_1 = \alpha_2 = \dots = \alpha_N = \alpha = 10.02$ and $\beta_1 = \beta_2 = \dots = \beta_N = \beta = 2.98$; and ii) the worst-case scenario, in which all the links experience strong turbulence, i.e., $\alpha_1 = \alpha_2 = \dots = \alpha_N = \alpha = 4.94$ and $\beta_1 = \beta_2 = \dots = \beta_N = \beta = 1.23$. As expected for given N and turbulence conditions, as ρ_s/ρ_{th} increases, the OP decreases. Moreover, for given N and ρ_s/ρ_{th} , as the turbulence intensity gets higher, the OP also increases. For example, for $N = 2$ and $\rho_s/\rho_{\text{th}} = 40$ dB, the OP increases for about 2 orders of magnitude, as we move from the best- to the worst-case scenario. Finally, for fixed turbulence conditions and ρ_s/ρ_{th} , as N increases, the impact of turbulence is multiplied; thus, the OP increases. For instance, for the best-case scenario and $\rho_s/\rho_{\text{th}} = 40$ dB, the OP increases for about one order of magnitude, as N increases from 2 to 3. This reveals the proliferative effect of turbulence in FSO systems that consists of multiple-RISs.

Figure 5 depicts the OP as a function of the σ_s/b for different values of b/w_d and $N = L$, assuming $\rho_s/\rho_{\text{th}} = 40$ dB. Notice that in the scenario under investigation, we assume all the same transmission and misalignment characteristics for all the links. Moreover, the following scenarios are examined:

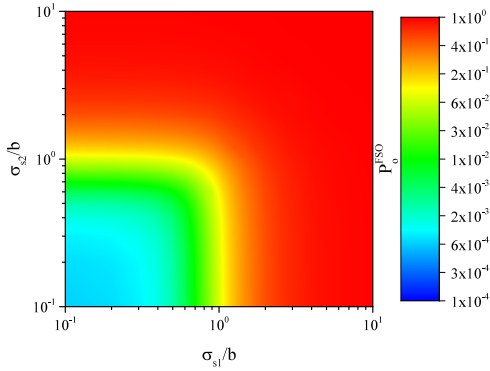


Fig. 6: OP vs σ_{s1}/β and σ_{s2}/β , for $N = L = 2$.

both RIS's and D lens radius are (i) half, (ii) equal to, and (iii) twice the radiation beam footprint. As a benchmark, the OP for the case in which there is no misalignment is also presented. As expected, for given $N = L$ and b/w_d , as σ_s/b increases, i.e., the misalignment intensity becomes more severe, the outage performance degrades. For example, for $N = L = 2$ and $b/w_d = 1$, the OP increases for more than one order of magnitude, as σ_s/b changes from 0.1 to 0.5. Likewise, for fixed σ_s/b and b/w_d , as $N = L$ increases, the joint effect of misalignment and turbulence becomes more severe; thus, the OP increases. Finally, for given $M = N$ and σ_s/b , as b/w_d increases, the beam-waist is constrained; as a result, an outage performance improvement is observed. Interestingly, even in the low- σ_s/b regime, if $b/w_d \leq 1$, there exists an OP gap between the two systems that consider and ignore the misalignment fading. This is because (4) does not account for the beam-waist. On the other hand, for $b/w_d > 1$, in the low- σ_s/b regime, the OP of the FSO system that suffers from misalignment fading tends to the one with misalignment fading immunity. This indicates the importance of taking into account b/w_d , when assessing the outage performance of RIS-empowered FSO systems.

Figure 6 demonstrates the impact of different levels of misalignment fading on the OP of a multi-RIS-empowered FSO system with $N = L = 2$. Specifically, the OP is presented as a function of σ_{s1}/b and σ_{s2}/b , assuming $\rho_s/\rho_{th} = 40$ dB, $\alpha_1 = \alpha_2 = 10.02$ and $\beta_1 = \beta_2 = 2.98$. As expected, for a given σ_{s1}/b , as σ_{s2}/b increases, the outage performance degrades. For example, for $\sigma_{s1}/b = 0.1$, as σ_{s2}/b changes from 0.1 to 0.6, the OP increases for approximately one order of magnitude. Similarly, for a fixed σ_{s2}/b , as σ_{s1}/b increases, the OP increases. This indicates that the performance of the multi-RIS-empowered FSO system is determined by the performance of its worst link. Finally, from this figure, we observe that a multi-RIS-empowered FSO system in which $\sigma_1/b = v_1$ and $\sigma_2/b = v_2$ achieves the same performance as the one with $\sigma_1/b = v_2$ and $\sigma_2/b = v_1$.

Figure 7 depicts the OP as a function of ρ_s/ρ_{th} for different values of N and L , assuming $\alpha_1 = \alpha_2 = \dots = \alpha_N = 10.02$ and $\beta_1 = \beta_2 = \dots = \beta_N = 2.98$. As expected, for fixed N and L , as ρ_s/ρ_{th} increases, the OP decreases. For instance, for $N = 3$ and $L = 2$, the outage performance improves for about one order of magnitude, as ρ_s/ρ_{th} increases from 20 to 35 dB. Additionally, for given L and ρ_s/ρ_{th} , performance degradation

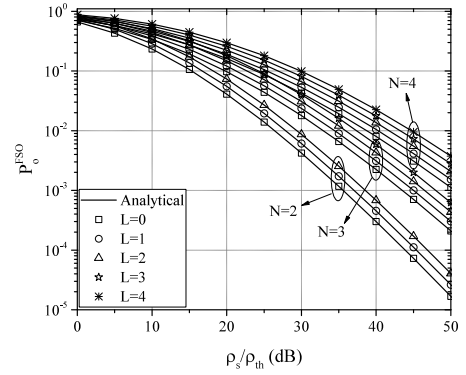


Fig. 7: OP vs ρ_s/ρ_{th} , for different values of N and L .

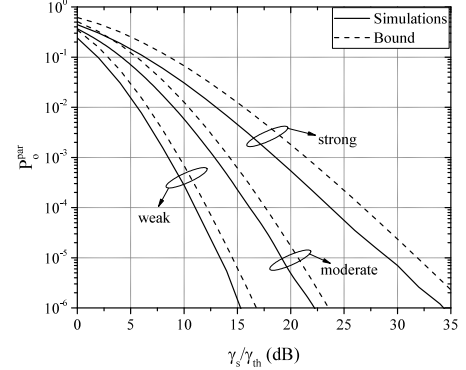


Fig. 8: OP vs ρ_s/ρ_{th} , for different levels of turbulence, assuming $N = L = 2$.

is observed as N increases. Finally, for given N and ρ_s/ρ_{th} , as L increases, the impact of misalignment becomes more severe; hence, the OP increases.

B. Parallel Multi-RIS FSO System

In Fig. 8, the OP of the parallel multi-RIS FSO system is presented as a function of ρ_s/ρ_{th} , for different turbulence conditions, assuming $N = L = 2$, $\sigma_{s1}/b = \sigma_{s2}/b = 0.1$ and $b/w_d = 0.5$. In this figure, continuous lines are used to denote results extracted from Monte Carlo simulations, while dashed-ones are obtained according to (38). It is observed that for a given turbulence condition, as ρ_s/ρ_{th} increases, the OP decreases. Moreover, from this figure, the upper bound is verified. Finally, it becomes apparent that, for a fixed ρ_s/ρ_{th} , as the turbulence intensity increases, the error between the simulation and upper bound increases. Despite this fact, the OP upper bound presented in (38) can become a useful tool for the design of parallel multi-RIS FSO systems.

Figure 9 illustrates the OP of parallel multi-RIS FSO system as a function of ρ_s/ρ_{th} , for different values of $N = L$, assuming $\alpha_i = 10.02$, $\beta_i = 2.98$, $\Omega_i = 1$, $\sigma_{si}/b_i = 0.1$ and $\beta_i/w_{di} = 0.5$ for $i \in [1, N]$. Again, continuous lines are used to denote results, which are extracted from simulations, while dashed-ones represent the OP upper bound, as derived from (38). As expected, for a fixed $N = L$, both the OP and its bound decreases, as ρ_s/ρ_{th} increases. Additionally, it is observed that for a given ρ_s/ρ_{th} , as $N = L$ increases, the diversity order increases; thus, outage performance improves. Meanwhile, as $N = L$ increases, the error between the simulations and the OP upper bound increases. Finally, from this figure, it becomes evident that the bound accurately

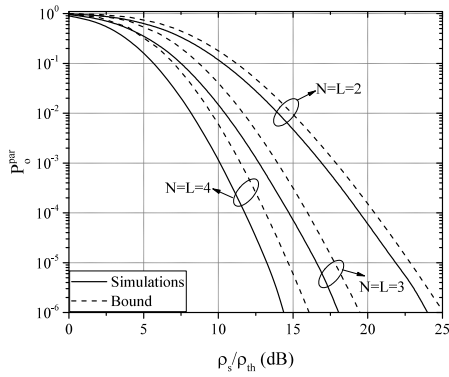


Fig. 9: OP vs ρ_s/ρ_{th} , for different values of $N = L$.

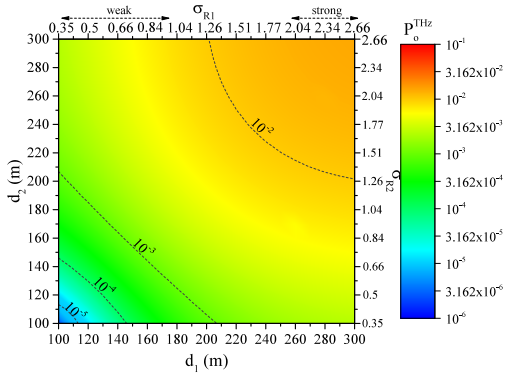


Fig. 10: OP vs d_1 and d_2 .

follows the simulations; as a consequence, it can be used to assess the outage performance ceiling of the parallel multi-RIS-empowered FSO system.

C. Cascaded RIS-empowered THz wireless systems

For the cascaded RIS-empowered THz wireless systems, we consider the following insightful scenario. Unless otherwise stated, $G_s = G_t = 50$ dBi, $R_i = 1$ for $i \in [1, N - 1]$ and $f = 300$ GHz. Additionally, standard atmospheric conditions, i.e., relative humidity, temperature, and pressure respectively equal to 50%, 296 °K, and 101325 Pa, are assumed. Under these atmospheric conditions, a realistic value for C_n^2 is $2.3 \times 10^{-9} \text{ m}^{-2/3}$ [95] and $\kappa(f) = 5.8268 \times 10^{-4}$.

Figure 10 quantifies the impact of turbulence on the outage performance of multi-RIS-empowered THz wireless systems in the absence of misalignment and hardware imperfections, assuming $N = 2$, $\gamma_s/\gamma_{th} = 25$ dB. In more detail, the OP is illustrated as a function of d_1 and d_2 . In this figure, for the sake of convenience, the corresponding values of σ_{R1} and σ_{R2} are respectively provided in the top horizontal and right vertical axes. Of note, according to [89], $\sigma_{Ri} < 1$, $1 < \sigma_{Ri} < 2$ and $\sigma_{Ri} > 2$ respectively correspond to weak, moderate, and strong turbulence conditions. As expected, for a fixed d_1 , as d_2 increases, σ_{R2} increases; thus, an outage performance degradation is observed. For example, for $d_1 = 100$ m, the OP increases by approximately one order of magnitude, as d_2 changes from 110 to 150 m. Similarly, for a given d_2 , as d_1 increases, σ_{R1} also increases, i.e., turbulence intensity increases; in turn, the OP increases. For instance, for $d_2 = 100$ m, the OP increases by about 10 times, as d_1 changes from 110 to 150 m. The aforementioned examples reveal that the system with $d_1 = v_1$ and $d_2 = v_2$ achieves the same outage

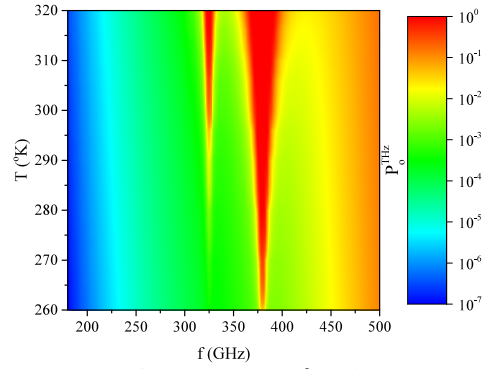


Fig. 11: OP vs f and T .

performance as the one with $d_1 = v_2$ and $d_1 = v_1$, where v_1 and v_2 are independent variables. Finally, from this figure, we observe that for a given e2e transmission distance, $d_1 + d_2$, the worst outage performance is observed for $d_1 = d_2$. For example, for $d_1 + d_2 = 300$ m, the OP for the case in which $d_1 = 100$ m and $d_2 = 200$ m is equal to 8.58×10^{-4} , while, for $d_1 = d_2 = 150$ m, it is 8.8×10^{-4} . Of note, this comes in line with the majorization theory [96].

Figure 11 illustrates the joint effect of molecular absorption and turbulence in terms of OP. In particular, the OP is plotted against the transmission frequency and temperature. The following insightful scenario is considered. The transmission power, bandwidth, B , and spectral efficiency of the transmission scheme are respectively set to 0 dBW, 50 GHz, and 2 bit/s/Hz, while N and L are respectively equal to 2 and 0. Moreover, $d_1 = d_2 = 100$ m and $\kappa_t = \kappa_r = 0$. At the destination side, we assumed that the low noise amplifier's gain and noise figure (NF) are 35 dB, and 1 dB, respectively. The mixer and miscellaneous losses are respectively 5 and 3 dB, whereas, the mixer's NF is 6 dB. The thermal noise power is evaluated as $N_1 = k_B T B$, where k_B is the Boltzman's constant. Note that the simulation parameters that we used in this work are inline with [97]. This figures shows that two molecular absorption "walls" exist around 325 and 380 GHz. Within the molecular absorption walls, the OP is higher than 10^{-2} . The length of these walls depends on the temperature. Specifically, as the temperature increases, the molecular absorption becomes more severe; as a result, the length of the molecular absorption walls also increases. Outside the aforementioned walls, in the 100 to 500 GHz band, there exist three transmission windows. Within these windows, for a fixed temperature, as the transmission frequency increases, the system outage performance degrades. Similarly, for a given transmission frequency, as the temperature increases, the OP also increases. It is worth noting that, within the transmission windows, the dominant phenomenon that affects the losses is free space propagation, while molecular absorption plays a secondary role.

Figure 12 quantifies the outage performance of multi-RIS empowered THz wireless systems in the presence of turbulence and misalignment, assuming that its transceivers are equipped with ideal RF front-end, i.e., $\kappa_t = \kappa_r = 0$, and the transmission distances for all the links are set to 100 m. Specifically, the OP is given as a function of σ_s , for different values of $N = L$ and γ_s/γ_{th} . Of note, in this

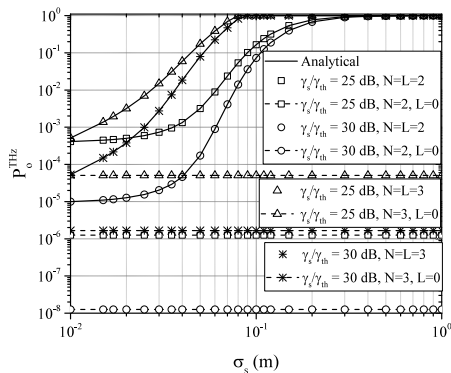


Fig. 12: OP vs σ_s , for different values of N , L and γ_s/γ_{th} .

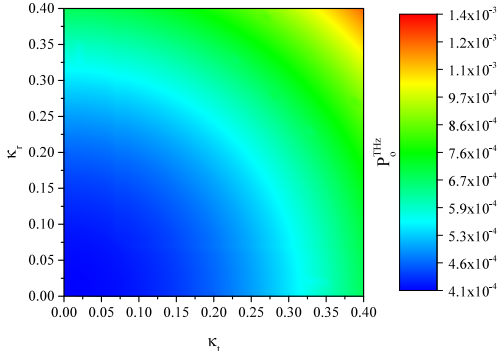


Fig. 13: OP vs κ_t and κ_r .

scenario, we assumed that $\sigma_{s,1} = \sigma_{s,2} = \dots = \sigma_{s,L} = \sigma_s$. As a benchmark, the OP in the absence of misalignment fading is also plotted. As expected, for given $N = L$ and γ_s/γ_{th} , the outage performance degrades, as the intensity of misalignment fading, i.e., σ_s , becomes more severe. For example, for $N = L = 3$ and $\gamma_s/\gamma_{th} = 30$ dB, the OP increases for about four orders of magnitude, as σ_s changes from 1 cm to 1 dm. Meanwhile, for fixed $N = L$ and σ_s , as γ_s/γ_{th} , the OP decreases. On the other hand, for given σ_s and γ_s/γ_{th} , as $N = L$ increases, the OP also increases. For instance, for $\sigma_s = 4$ cm and $\gamma_s/\gamma_{th} = 25$ dB, the OP increases by approximately 10 times, as $N = L$ changes from 2 to 3. Finally, from this figure, the detrimental impact of misalignment fading becomes apparent by comparing; thus, the importance of accurately characterizing the channels of the RIS-empowered THz wireless systems is highlighted.

Figure 13 illustrates the impact of hardware imperfections in multi-RIS-empowered THz wireless systems, assuming $L = M = 2$, $d_1 = d_2 = 100$ m, $\sigma_1 = \sigma_2 = 1$ mm and $\gamma_s/\gamma_{th} = 25$ dB. Of note the case in which $\kappa_t = \kappa_r = 0$ corresponds to the best-case scenario, in which both the S and D are equipped with ideal RF front-ends. We observe that, for a given κ_t , as κ_r increases, the OP also increases. Similarly, for a fixed κ_t , an outage performance degradation occurs, when κ_r increases. Additionally, for a constant $\kappa_t + \kappa_r$, we observe that the OP is maximized for $\kappa_t = \kappa_r$. Finally, it is verified that systems with the same $\kappa_t^2 + \kappa_r^2$ achieve the same outage performance.

In Fig. 14, the OP is presented as a function of γ_s for different values of $\sigma_1 = \sigma_2 = \sigma_s$, γ_{th} as well as κ_t and κ_r , assuming $N = L = 2$ and $d_1 = d_2 = 100$ m. In particular, the ideal ($\kappa_t = \kappa_r = 0$), best ($\kappa_t = \kappa_r = 0.1$) and worst ($\kappa_t = \kappa_r = 0.4$) practical cases from the hardware imperfections

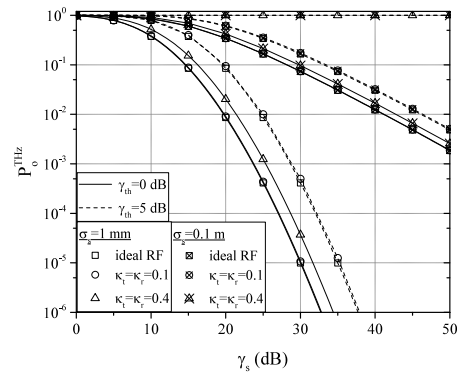


Fig. 14: OP vs γ_s , for different values of γ_{th} , σ_s , κ_t and κ_r .

point of view are illustrated. As expected, for given $\gamma_{th} \leq \frac{1}{\kappa_t^2 + \kappa_r^2}$, κ_t , κ_r and σ_s , as γ_s increases, the OP decreases. For example, for ideal RF front-end, $\gamma_{th} = 0$ dB and $\sigma_s = 1$ mm, the OP decreases by 100 times, as γ_s changes from 20 to 30 dB. On the other hand, as predicted by (58), the OP is equal to 1. Meanwhile, for fixed $\gamma_{th} \leq \frac{1}{\kappa_t^2 + \kappa_r^2}$, κ_t , κ_r and γ_s , as σ_s increases, the OP also increases. For instance, for $\kappa_t = \kappa_r = 0.1$, $\gamma_{th} = 0$ dB and $\gamma_s = 20$ dB, the outage performance degrades by about one order of magnitude, as σ_s increases from 1 mm to 0.1 m. This example highlights the significance of the impact of misalignment fading in multi-RIS-empowered THz wireless systems. Likewise, for given σ_s , κ_t , κ_r and γ_s , a γ_{th} increase causes an OP increase. Finally, the impact of hardware imperfections in systems operating at higher γ_{th} is more severe than the ones working in lower γ_{th} . Since γ_{th} is connected with the transmission scheme's spectral efficiency, the impact of hardware imperfections can be constrained by selecting transmission schemes of low-spectral efficiency.

V. CONCLUSIONS

In this paper, we introduced a theoretical framework for the statistical characterization of cascaded composite turbulence and misalignment channels in terms of PDF and CDF. Moreover, we assessed the outage performance of cascaded multi-RIS FSO and THz systems in the presence of misalignment and turbulence by computing novel closed-form expressions for their OP. Additionally, we provided an insightful upper bound for parallel multi-RIS FSO systems. Our results revealed that in cascaded multi-RIS FSO and THz systems, as the number of RIS and thus the distance between S and D increases, the turbulence and misalignment fading intensity becomes more severe; as a result, the outage performance degrades. On the other hand, in parallel multi-RIS FSO systems, as the number of links increases, the diversity order also increases; hence, the OP decreases. Likewise, the impact of unavoidable transceivers' hardware imperfections on the outage performance of cascaded multi-RIS THz systems was quantified. Finally, the importance of accurately characterizing the transmission medium was emphasized.

APPENDICES

APPENDIX A

PROOF OF THEOREM 2

In order to prove that the PDF of Z_2 can be expressed as in (7), we use the induction method [98]. First, we prove

that (7) holds for $L = 2$. In this case, since l_1 and l_2 are independent, the PDF of Z_2 can be evaluated as

$$f_{Z_2}(x; L = 2) = \int_{\frac{x}{A_{o,1}}}^{A_{o,2}} \frac{1}{y} f_{l_1}\left(\frac{x}{y}\right) f_{l_2}(y) dy. \quad (62)$$

By applying (6) in (62), we obtain

$$f_{Z_2}(x; L = 2) = \frac{\xi_1 \xi_2}{A_{o,1}^{\xi_1} A_{o,2}^{\xi_2}} x^{\xi_1-1} \int_{\frac{x}{A_{o,1}}}^{A_{o,2}} y^{-1} dy, \quad (63)$$

which, according to [73, eq. (2.01/2)], can be rewritten as

$$f_{Z_2}(x; L = 2) = \frac{\prod_{i=1}^2 \xi_i}{\prod_{i=1}^2 A_{o,i}^{\xi_i}} x^{\xi_1-1} \ln\left(\frac{\prod_{i=1}^2 A_{o,i}}{x}\right), \quad (64)$$

for $0 \leq x \leq A_{o,1} A_{o,2}$. By comparing (64) with (7), it becomes evident that (7) is true for $L = 2$.

Next, for $L = 3$, since l_1 , l_2 , and l_3 are independent, the PDF of Z_2 can be obtained as

$$f_{Z_2}(x; L = 3) = \int_{\frac{x}{A_{o,3}}}^{\prod_{i=1}^2 A_{o,i}} \frac{1}{y} f_{Z_2}(y; L = 2) f_{l_3}\left(\frac{x}{y}\right) dy, \quad (65)$$

which, with the aid of (6) and (64), can be rewritten as

$$f_{Z_2}(x; L = 3) = \prod_{i=1}^3 \frac{\xi_i}{A_{o,i}^{\xi_i}} x^{\xi_3-1} \times \int_{\frac{x}{A_{o,3}}}^{\prod_{i=1}^2 A_{o,i}} y^{-1} \ln\left(\frac{\prod_{i=1}^2 A_{o,i}}{y}\right) dy. \quad (66)$$

Next, by applying [73, eq. (2.721/3)] in (66), we get

$$f_{Z_2}(x; L = 3) = \frac{1}{2} \frac{\prod_{i=1}^3 \xi_i x^{\xi_3-1}}{\prod_{i=1}^3 A_{o,i}^{\xi_i}} \left(\ln\left(\frac{\prod_{i=1}^3 A_{o,i}}{x}\right) \right)^2, \quad (67)$$

with $0 \leq x \leq A_{o,3}^3$.

Let us assume that (7) holds for $L = M$, i.e.,

$$f_{Z_2}(x; L = M) = \frac{1}{(M-1)!} \frac{\prod_{i=1}^M \xi_i}{\prod_{i=1}^M A_{o,i}^{\xi_i}} x^{\xi_M-1} \times \left(\ln\left(\frac{\prod_{i=1}^M A_{o,i}}{x}\right) \right)^{M-1}. \quad (68)$$

Then, for $L = M + 1$, the PDF of Z_2 can be evaluated as

$$f_{Z_2}(x; L = M + 1) = \int_{\frac{x}{A_o}}^{A_o^M} \frac{f_{Z_2}(y; L = M) f_{l_{M+1}}\left(\frac{x}{y}\right)}{y} dy, \quad (69)$$

which, by applying (6) and (68), can be rewritten as

$$f_{Z_2}(x; L = M + 1) = \frac{x^{\xi-1}}{(M-1)!} \left(\frac{\xi}{A_o}\right)^{M+1} \times \int_{\frac{x}{A_o}}^{A_o^M} \left(\ln\left(\frac{A_o^M}{y}\right)\right)^{M-1} dy. \quad (70)$$

By applying [73, eq. (2.721/1)], (70) can be written in a closed-form as

$$f_{Z_2}(x; L = M + 1) = \frac{1}{M!} \frac{\prod_{i=1}^{M+1} \xi_i}{\prod_{i=1}^{M+1} A_{o,i}^{\xi_i}} x^{\xi_{M+1}-1} \times \left(\ln\left(\frac{\prod_{i=1}^M A_{o,i}}{x}\right) \right)^M, \quad (71)$$

with $0 \leq x \leq x^{M+1}$. Notice, that from (71), it becomes apparent that if (7) holds for $L = M$, it also holds for $L = M + 1$. Since it also holds for $N - 2$, then it stands for each $N \geq 2$. This concludes the proof.

APPENDIX B

PROOF OF THEOREM 3

Since $L \leq N$, with the aid of (3) and (5), (9) can be rewritten as

$$Z = Y_1 Y_2, \quad (72)$$

where

$$Y_1 = \prod_{i=1}^L r_i l_i \quad \text{and} \quad Y_2 = \prod_{i=L+1}^N r_i. \quad (73)$$

To extract a closed-form expression for the PDF of Z , we need first to evaluate the PDF of Y_1 . In this direction, let us assume that $L = 1$; then, the PDF of Y_1 yields as

$$f_{Y_1}(x; L = 1) = \int_{\frac{x}{A_{o,1}}}^{\infty} \frac{1}{y} f_{r_1}(y) f_{l_1}\left(\frac{x}{y}\right) dx, \quad (74)$$

which, by applying (2) and (6), can be rewritten as

$$f_{Y_1}(x; L = 1) = 2 \left(\frac{\alpha_1 \beta_1}{\Omega_1} \right)^{\frac{\alpha_1 + \beta_1}{2}} \frac{1}{\Gamma(\alpha_1) \Gamma(\beta_1) A_{o,1}^{\xi_1}} x^{\xi_1-1} \times \int_{\frac{x}{A_o}}^{\infty} y^{\frac{\alpha_1 + \beta_1}{2} - 1 - \xi_1} K_{\alpha_1 - \beta_1} \left(2 \sqrt{\frac{\alpha_1 \beta_1 y}{\Omega_1}} \right) dy. \quad (75)$$

By employing [99, ch. 2.6], (75) can be written as in (76), given at the top of the next page. Additionally, by applying [77, eq. (2.24.5/3)], (76) can be analytically expressed as

$$f_{Y_1}(x; L = 1) = \left(\frac{\alpha_1 \beta_1}{\Omega_1 A_{o,1}} \right)^{\frac{\alpha_1 + \beta_1}{2}} \frac{\xi_1}{\Gamma(\alpha_1) \Gamma(\beta_1)} x^{\frac{\alpha_1 + \beta_1}{2} - 1} \times G_{1,3}^{3,0} \left(\frac{\alpha_1 \beta_1 x}{A_o \Omega_1} \left| \begin{array}{c} -\frac{\alpha_1 + \beta_1}{2} + \xi_1 + 1 \\ \frac{\alpha_1 - \beta_1}{2}, -\frac{\alpha_1 - \beta_1}{2}, -\frac{\alpha_1 + \beta_1}{2} + \xi_1 \end{array} \right. \right), \quad (77)$$

which, with the aid of [100], can be rewritten as

$$f_{Y_1}(x; L = 1) = \frac{\xi_1 x^{-1}}{\Gamma(\alpha_1) \Gamma(\beta_1)} G_{1,3}^{3,0} \left(\frac{\alpha_1 \beta_1 x}{A_{o,1} \Omega_1} \left| \begin{array}{c} \xi_1 + 1 \\ \alpha_1, \beta_1, \xi_1 \end{array} \right. \right). \quad (78)$$

For $L = 2$, the PDF of Y_1 can be obtained as

$$f_{Y_1}(x; L = 2) = \int_0^{\infty} \frac{1}{y} f_{Y_1}(y; L = 1) f_{Y_1}\left(\frac{x}{y}; L = 1\right) dy, \quad (79)$$

which, by applying (78), can be rewritten as in (80), given at the top of the next page. By employing [73, eq. (9.31/1)], we can write (80) as in (81), given at the top of the next page. Finally, by applying [77, eq. (2.24.5/3)] in (81), we get

$$f_{Y_1}(x; L = 2) = \frac{\prod_{i=1}^2 \xi_i}{\prod_{i=1}^2 \Gamma(\alpha_i) \Gamma(\beta_i)} x^{-1} \times G_{2,6}^{6,0} \left(\frac{\prod_{i=1}^2 \alpha_i \beta_i}{A_{o,1} \prod_{i=1}^2 \Omega_i} y \left| \begin{array}{c} \xi_1 + 1, \xi_2 + 1 \\ \alpha_1, \beta_1, \xi_1, \alpha_2, \beta_2, \xi_2 \end{array} \right. \right). \quad (82)$$

By recurrently conducting this procedure, for $L = 3, 4, \dots$, we prove that $f_{Y_1}(x)$ can be obtained as in (83), given at the top of the next page.

Moreover, by following the same steps as in Appendix B, it can be proven that the PDF of Y_2 can be obtained as in (84), given at the top of the next page. Thus, since Y_1 and Y_2 are independent, the PDF of Z occurs as

$$f_Z(x) = \int_0^{\infty} \frac{1}{y} f_{Y_1}(y) f_{Y_2}\left(\frac{x}{y}\right) dy, \quad (85)$$

which by substituting (83) and (84), can be written as in (86), given at the top of the next page. By employing [100], (86) can be rewritten in a closed-form as in (87), given at the top of the next page. Finally, by employing [77, eq. (2.24.5/3)],

$$f_{Y_1}(x; L = 1) = \left(\frac{\alpha_1 \beta_1}{\Omega_1} \right)^{\frac{\alpha_1 + \beta_1}{2}} \frac{1}{\Gamma(\alpha_1) \Gamma(\beta_1)} \frac{\xi}{A_{o,1}^{\xi_1}} x^{\xi_1 - 1} \int_{\frac{x}{A_{o,1}}}^{\infty} \left(\frac{1}{y} \right)^{-\frac{\alpha_1 + \beta_1}{2} + \xi_1 + 1} G_{0,2}^{2,0} \left(\frac{\alpha_1 \beta_1 y}{\Omega_1} \middle| \frac{\alpha_1 - \beta_1}{2}, -\frac{\alpha_1 - \beta_1}{2} \right) dy \quad (76)$$

$$f_{Y_1}(x; L = 2) = \frac{\prod_{i=1}^2 \xi_i}{\prod_{i=1}^2 \Gamma(\alpha_i) \Gamma(\beta_i)} x^{-1} \int_0^{\infty} y^{-1} G_{1,3}^{3,0} \left(\frac{\alpha_1 \beta_1 y}{A_{o,1} \Omega_1} \middle| \xi_1 + 1 \right) G_{1,3}^{3,0} \left(\frac{\alpha_2 \beta_2 x}{A_{o,2} \Omega_2 y} \middle| \xi_2 + 1 \right) dy \quad (80)$$

$$f_{Y_1}(x; L = 2) = \frac{\prod_{i=1}^2 \xi_i}{\prod_{i=1}^2 \Gamma(\alpha_i) \Gamma(\beta_i)} x^{-1} \int_0^{\infty} y^{-1} G_{1,3}^{3,0} \left(\frac{\alpha_1 \beta_1 y}{A_{o,1} \Omega_1} \middle| \xi_1 + 1 \right) G_{3,1}^{0,3} \left(\frac{A_{o,2} \Omega_2 y}{\alpha_2 \beta_2 x} \middle| \begin{matrix} 1 - \alpha_2, 1 - \beta_2, 1 - \xi_2 \\ 1 - \xi_2 \end{matrix} \right) dy \quad (81)$$

$$f_{Y_1}(x) = \frac{\prod_{i=1}^L \xi_i}{\prod_{i=1}^L \Gamma(\alpha_i) \Gamma(\beta_i)} x^{-1} G_{L,3L}^{3L,0} \left(\frac{\prod_{i=1}^L \alpha_i \beta_i}{\prod_{i=1}^L \Omega_i A_{o,i}} x \middle| \begin{matrix} \xi_1 + 1, \xi_2 + 1, \dots, \xi_L + 1 \\ \alpha_1, \dots, \alpha_L, \beta_1, \dots, \alpha_L, \xi_1, \xi_2, \dots, \xi_L \end{matrix} \right). \quad (83)$$

we get (10).

The CDF of Z can be evaluated as

$$F_Z(x) = \int_0^x f_Z(y) dy, \quad (88)$$

which, by applying [77, eq. (2.24.5/3)], returns (11). This concludes the proof.

REFERENCES

- [1] M. Latva-aho, K. Leppänen, F. Clazzer, and A. Munari, "Key drivers and research challenges for 6G ubiquitous wireless intelligence," *White Paper*, 2020.
- [2] L. Bariah, L. Mohjazi, S. Muhaidat, P. C. Sofotasios, G. K. Kurt, H. Yanikomeroglu, and O. A. Dobre, "A prospective look: Key enabling technologies, applications and open research topics in 6G networks," *IEEE Access*, vol. 8, pp. 174 792–174 820, Aug. 2020.
- [3] A.-A. A. Boulogeorgos, A. Alexiou, D. Kritharidis, A. Katsiotis, G. Ntouni, J. Kokkonemi, J. Lethtomaki, M. Juntti, D. Yankova, A. Mokhtar, J.-C. Point, J. Machodo, R. Elschner, C. Schubert, T. Merkle, R. Ferreira, F. Rodrigues, and J. Lima, "Wireless terahertz system architectures for networks beyond 5G," TERRANOVA CONSORTIUM, White paper 1.0, Jul. 2018.
- [4] S. Dang, O. Amin, B. Shihada, and M.-S. Alouini, "What should 6G be?" *Nature Electronics*, vol. 3, no. 1, pp. 20–29, Jan. 2020.
- [5] A.-A. A. Boulogeorgos, A. Alexiou, T. Merkle, C. Schubert, R. Elschner, A. Katsiotis, P. Stavrianos, D. Kritharidis, P. K. Chartsias, J. Kokkonemi, M. Juntti, J. Lehtomäki, A. Teixeira, and F. Rodrigues, "Terahertz technologies to deliver optical network quality of experience in wireless systems beyond 5G," *IEEE Commun. Mag.*, vol. 56, no. 6, pp. 144–151, Jun. 2018.
- [6] Z. Zhang, Y. Xiao, Z. Ma, M. Xiao, Z. Ding, X. Lei, G. K. Karagiannidis, and P. Fan, "6G wireless networks: Vision, requirements, architecture, and key technologies," *IEEE Veh. Technol. Mag.*, vol. 14, no. 3, pp. 28–41, sep 2019.
- [7] I. F. Akyildiz, A. Kak, and S. Nie, "6G and beyond: The future of wireless communications systems," *IEEE Access*, vol. 8, pp. 133 995–134 030, Jul. 2020.
- [8] A.-A. A. Boulogeorgos and A. Alexiou, "Error analysis of mixed THz-RF wireless systems," *IEEE Commun. Lett.*, vol. 24, no. 2, pp. 277–281, feb 2020.
- [9] N. Chi, Y. Zhou, Y. Wei, and F. Hu, "Visible light communication in 6G: Advances, challenges, and prospects," *IEEE Veh. Technol. Mag.*, vol. 15, no. 4, pp. 93–102, Dec. 2020.
- [10] P. Porambage, G. Gur, D. P. M. Osorio, M. Liyanage, A. Gurtov, and M. Ylianttila, "The roadmap to 6G security and privacy," *IEEE Open Journal of the Communications Society*, vol. 2, pp. 1094–1122, May 2021.
- [11] M. A. Arfaoui, M. D. Soltani, I. Tavakkolnia, A. Ghrayeb, C. M. Assi, M. Safari, and H. Haas, "Measurements-based channel models for indoor LiFi systems," *IEEE Trans. Wireless Commun.*, vol. 20, no. 2, pp. 827–842, Feb. 2021.
- [12] M. Di Renzo, M. Debbah, D.-T. Phan-Huy, A. Zappone, M.-S. Alouini, C. Yuen, V. Sciancalepore, G. C. Alexandropoulos, J. Hoydis, H. Gacanin, J. d. Rosny, A. Bounceur, G. Lerosey, and M. Fink, "Smart radio environments empowered by reconfigurable ai metasurfaces: An idea whose time has come," *EURASIP Journal on Wireless Communications and Networking*, vol. 2019, no. 1, pp. 1–20, May 2019.
- [13] M. Di Renzo, A. Zappone, M. Debbah, M.-S. Alouini, C. Yuen, J. de Rosny, and S. Tretyakov, "Smart radio environments empowered by reconfigurable intelligent surfaces: How it works, state of research, and the road ahead," *IEEE J. Sel. Areas Commun.*, vol. 38, no. 11, pp. 2450–2525, nov 2020.
- [14] O. Tsilipakos, A. C. Tasolamprou, A. Pitilakis, F. Liu, X. Wang, M. S. Mirmoosa, D. C. Tzarouchis, S. Abadal, H. Taghvaei, C. Liaskos, A. Tsioliariidou, J. Georgiou, A. Cabellos-Aparicio, E. Alarcón, S. Ioannidis, A. Pitsillides, I. F. Akyildiz, N. V. Kantartzis, E. N. Economou, C. M. Soukoulis, M. Kafesaki, and S. Tretyakov, "Toward intelligent metasurfaces: The progress from globally tunable metasurfaces to software-defined metasurfaces with an embedded network of controllers," *Adv. Opt. Mater.*, vol. 8, no. 17, p. 2000783, Jul. 2020.
- [15] A.-A. A. Boulogeorgos and A. Alexiou, "Performance analysis of reconfigurable intelligent surface-assisted wireless systems and comparison with relaying," *IEEE Access*, vol. 8, pp. 94 463–94 483, 2020.
- [16] S. Koenig, D. Lopez-Diaz, J. Antes, F. Boes, R. Henneberger, A. Leuther, A. Tessmann, R. Schmogrow, D. Hillerkuss, R. Palmer, T. Zwick, C. Koos, W. Freude, O. Ambacher, J. Leuthold, and I. Kallfass, "Wireless sub-THz communication system with high data rate," *Nat. Photonics*, vol. 7, pp. 977 EP–, Oct. 2013.
- [17] G. Parca, "Optical wireless transmission at 1.6-Tbit/s (16×100 Gbit/s) for next-generation convergent urban infrastructures," *Opt. Eng.*, vol. 52, no. 11, p. 116102, Nov. 2013.
- [18] M. A. Esmail, A. Ragheb, H. Fathallah, and M.-S. Alouini, "Experimental demonstration of outdoor 2.2 Tbps super-channel FSO transmission system," in *IEEE International Conference on Communications Workshops (ICC)*. IEEE, May 2016.
- [19] M. V. Mazurczyk, J.-X. Cai, M. Paskov, W. W. Patterson, O. V. Sinkin, Y. Hu, C. R. Davidson, P. C. Corbett, T. E. Hammon, M. A. Bolshtyansky, D. G. Foursa, and A. N. Pilipetskii, "Demonstration of 3,010 km WDM transmission in 3.83 THz bandwidth using SOAs," in *Optical Fiber Communications Conference and Exhibition (OFC)*, Mar. 2020, pp. 1–3.
- [20] C. Jastrow, S. Priebe, B. Spitschan, J. Hartmann, M. Jacob, T. Kurner, T. Schrader, and T. Kleine-Ostmann, "Wireless digital data transmission at 300 GHz," *Electron. Lett.* 10.1007/s10762-014-0140-6, vol. 46, no. 9, p. 661, 2010.
- [21] I. Kallfass, F. Boes, T. Messinger, J. Antes, A. Inam, U. Lewark, A. Tessmann, and R. Henneberger, "64 Gbit/s transmission over 850 m fixed wireless link at 240 GHz carrier frequency," *J. Infrared Millim. Terahertz Waves*, vol. 36, no. 2, pp. 221–233, Jan. 2015.
- [22] C. Castro, R. Elschner, T. Merkle, C. Schubert, and R. Freund, "Experimental demonstrations of high-capacity THz-wireless transmission systems for beyond 5g," *IEEE Commun. Mag.*, vol. 58, no. 11, pp. 41–47, Nov. 2020.
- [23] A.-A. A. Boulogeorgos, J. M. Jornet, and A. Alexiou, "A quantitative look at directional terahertz communication systems for 6g: Fact check," *IEEE Veh. Technol. Mag.*, vol. 16, no. 4, Oct. 2021.

$$f_{Y_2}(x) = \frac{G_{0,2(N-L)}^{2(N-L),0} \left[x \prod_{i=L+1}^N \frac{\alpha_i \beta_i}{\Omega_i} \middle| \alpha_{L+1}, \beta_{L+1}, \alpha_{L+2}, \beta_{L+2} \cdots, \alpha_N, \beta_N \right]}{x \prod_{i=L+1}^N \Gamma(\alpha_i) \Gamma(\beta_i)}. \quad (84)$$

$$f_Z(x) = \frac{\prod_{i=1}^L \xi_i}{\prod_{i=1}^N \Gamma(\alpha_i) \Gamma(\beta_i)} x^{-1} \int_0^\infty y^{-1} G_{L,3L}^{3L,0} \left(\frac{\prod_{i=1}^L \alpha_i \beta_i}{\prod_{i=1}^L \Omega_i A_{o,i}} y \middle| \xi_1 + 1, \xi_2 + 1, \cdots, \xi_L + 1 \right. \\ \left. \alpha_1, \cdots, \alpha_L, \beta_1, \cdots, \alpha_L, \xi_1, \xi_2, \cdots, \xi_L \right) \\ \times G_{0,2(N-L)}^{2(N-L),0} \left(\frac{x}{y} \prod_{i=L+1}^N \frac{\alpha_i \beta_i}{\Omega_i} \middle| \alpha_{L+1}, \beta_{L+1}, \alpha_{L+2}, \beta_{L+2} \cdots, \alpha_N, \beta_N \right) dy \quad (86)$$

$$f_Z(x) = \frac{\xi^L}{\prod_{i=1}^N \Gamma(\alpha_i) \Gamma(\beta_i)} x^{-1} \int_0^\infty y^{-1} G_{L,3L}^{3L,0} \left(\frac{\prod_{i=1}^L \alpha_i \beta_i}{\prod_{i=1}^L \Omega_i A_{o,i}} y \middle| \xi_1 + 1, \xi_2 + 1, \cdots, \xi_L + 1 \right. \\ \left. \alpha_1, \cdots, \alpha_L, \beta_1, \cdots, \alpha_L, \xi_1, \xi_2, \cdots, \xi_L \right) \\ \times G_{0,2(N-L)}^{0,2(N-L),0} \left(\frac{y}{x} \prod_{i=L+1}^N \frac{\Omega_i}{\alpha_i \beta_i} \middle| 1 - \alpha_{L+1}, 1 - \beta_{L+1}, 1 - \alpha_{L+2}, 1 - \beta_{L+2} \cdots, 1 - \alpha_N, 1 - \beta_N \right) dy \quad (87)$$

- [24] A.-A. A. Boulogeorgos, E. N. Papatotiriou, J. Kokkonemi, J. Lehtomäki, A. Alexiou, and M. Juntti, "Performance evaluation of THz wireless systems operating in 275-400 GHz band," *IEEE Vehicular Technology Conference (VTC)*, 2018.
- [25] R. Elschnner, C. Castro, R. Ferreira, T. Merkle, A. Alexiou, D. Kritharidis, J. Kokkonemi, and A.-A. A. Boulogeorgos, "D6.2-THz high-capacity demonstrator implementation report," TERRANOVA, Tech. Rep., 2020.
- [26] F. Rodrigues, R. Ferreira, C. Castro, G. Ntouni, R. Elschnner, T. Merkle, A.-A. A. Boulogeorgos, J. Kokkonemi, and A. Alexiou, "D6.3-TERRANOVA proof-of-concept test and validation report," TERRANOVA, resreport, Mar. 2020.
- [27] A. Elzanaty and M.-S. Alouini, "Adaptive coded modulation for IM/DD free-space optical backhauling: A probabilistic shaping approach," *IEEE Trans. Commun.* 10.1109/MCOM.2017.1600735, vol. 68, no. 10, pp. 6388–6402, Oct. 2020.
- [28] M. Alzenad, M. Z. Shakir, H. Yanikomeroglu, and M.-S. Alouini, "FSO-based vertical backhaul/fronthaul framework for 5G+ wireless networks," *IEEE Commun. Mag.*, vol. 56, no. 1, pp. 218–224, Jan. 2018.
- [29] M. A. Esmail, A. Ragheb, H. Fathallah, and M.-S. Alouini, "Investigation and demonstration of high speed full-optical hybrid FSO/fiber communication system under light sand storm condition," vol. 9, no. 1, pp. 1–12, Feb. 2017.
- [30] D. McDonald, R. Bellosi, S. Gladysz, and A. Lambert, "Demonstration of GBit/s coherent free-space optical communications over an 800 m outdoor path," in *Environmental Effects on Light Propagation and Adaptive Systems IV*, K. Stein and S. Gladysz, Eds. SPIE, Sep. 2021.
- [31] C. Zhang, K. Ota, J. Jia, and M. Dong, "Breaking the blockage for big data transmission: Gigabit road communication in autonomous vehicles," *IEEE Commun. Mag.*, vol. 56, no. 6, pp. 152–157, Jun. 2018.
- [32] A.-A. A. Boulogeorgos, S. Goudos, and A. Alexiou, "Users association in ultra dense THz networks," in *IEEE International Workshop on Signal Processing Advances in Wireless Communications (SPAWC)*, Kalamata, Greece, Jun. 2018.
- [33] G. T. Djordjevic, M. I. Petkovic, M. Spasic, and D. S. Antic, "Outage capacity of FSO link with pointing errors and link blockage," *Opt. Express*, vol. 24, no. 1, p. 219, Jan. 2016.
- [34] H. Kaushal and G. Kaddoum, "Optical communication in space: Challenges and mitigation techniques," *IEEE Communications Surveys & Tutorials*, vol. 19, no. 1, pp. 57–96, 2017.
- [35] C. Liaskos, *Internet of materials*. S.I: CRC PRESS, 2020.
- [36] M. Di Renzo, K. Ntontin, J. Song, F. H. Danufane, X. Qian, F. Lazarakis, J. de Rosny, D.-T. Phan-Huy, O. Simeone, R. Zhang, M. Debbah, G. Lerosey, M. Fink, S. Tretyakov, and S. Shamai, "Reconfigurable intelligent surfaces vs. relaying: Differences, similarities, and performance comparison," *IEEE Open Journal of the Communications Society*, pp. 1–1, 2020.
- [37] W. Tang, J. Y. Dai, M. Z. Chen, K.-K. Wong, X. Li, X. Zhao, S. Jin, Q. Cheng, and T. J. Cui, "MIMO transmission through reconfigurable intelligent surface: System design, analysis, and implementation," *IEEE J. Sel. Areas Commun.*, vol. 38, no. 11, pp. 2683–2699, Nov. 2020.
- [38] H. Taghvaei, S. Abadal, A. Ptilakis, O. Tsilipakos, A. C. Tasolamprou, C. Liaskos, M. Kafesaki, N. V. Kantartzis, A. Cabellos-Aparicio, and E. Alarcon, "Scalability analysis of programmable metasurfaces for beam steering," *IEEE Access*, vol. 8, pp. 105 320–105 334, 2020.
- [39] G. Zhou, C. Pan, H. Ren, K. Wang, M. El-kashlan, and M. Di Renzo, "Stochastic learning-based robust beamforming design for RIS-aided millimeter-wave systems in the presence of random blockages," *IEEE Trans. Veh. Technol.*, vol. 70, no. 1, pp. 1057–1061, Jan. 2021.
- [40] C. Pan, H. Ren, K. Wang, J. F. Kolb, M. El-kashlan, M. Chen, M. Di Renzo, Y. Hao, J. Wang, A. L. Swindlehurst, X. You, and L. Hanzo, "Reconfigurable intelligent surfaces for 6G systems: Principles, applications, and research directions," *ArXiv*, Nov. 2020.
- [41] J. H. Lee, J. W. Yoon, M. J. Jung, J. K. Hong, S. H. Song, and R. Magnusson, "A semiconductor metasurface with multiple functionalities: A polarizing beam splitter with simultaneous focusing ability," *Appl. Phys. Lett.*, vol. 104, no. 23, p. 233505, Jun. 2014.
- [42] S. Li, B. Duo, X. Yuan, Y.-C. Liang, and M. Di Renzo, "Reconfigurable intelligent surface assisted UAV communication: Joint trajectory design and passive beamforming," *IEEE Wireless Commun. Lett.*, vol. 9, no. 5, pp. 716–720, May 2020.
- [43] H. Cai, S. Chen, C. Zou, Q. Huang, Y. Liu, X. Hu, Z. Fu, Y. Zhao, H. He, and Y. Lu, "Multifunctional hybrid metasurfaces for dynamic tuning of terahertz waves," *Adv. Opt. Mater.*, vol. 6, no. 14, p. 1800257, May 2018.
- [44] J. Shabanpour, S. Beyraghi, and A. Cheldavi, "Ultrafast reprogrammable multifunctional vanadium-dioxide-assisted metasurface for dynamic THz wavefront engineering," *Sci. Rep.*, vol. 10, no. 1, Jun. 2020.
- [45] S. Venkatesh, X. Lu, H. Saeidi, and K. Sengupta, "A high-speed programmable and scalable terahertz holographic metasurface based on tiled CMOS chips," *Nature Electronics*, vol. 3, no. 12, pp. 785–793, Dec. 2020.
- [46] M. Amin, O. Siddiqui, H. Abutarboush, M. Farhat, and R. Ramzan, "A THz graphene metasurface for polarization selective virus sensing," *Carbon*, vol. 176, pp. 580–591, May 2021.
- [47] M. Tal, S. Keren-Zur, and T. Ellenbogen, "Nonlinear plasmonic metasurface terahertz emitters for compact terahertz spectroscopy systems," *ACS Photonics*, vol. 7, no. 12, pp. 3286–3290, Nov. 2020.
- [48] M. Ojaroudi and V. Loscri, "Graphene-based reconfigurable intelligent meta-surface structure for THz communications," in *15th European Conference on Antennas and Propagation (EuCAP)*. IEEE, Mar. 2021.
- [49] M. Manjappa, P. Pitchappa, N. Singh, N. Wang, N. I. Zheludev, C. Lee, and R. Singh, "Reconfigurable MEMS Fano metasurfaces with multiple-input-output states for logic operations at terahertz frequencies," *Nat Commun*, vol. 9, no. 1, Oct. 2018.
- [50] P. Brandl, S. Schidl, A. Polzer, W. Guberl, and H. Zimmermann, "Optical wireless communication with adaptive focus and MEMS-based beam steering," *IEEE Photon. Technol. Lett.*, vol. 25, no. 15, pp. 1428–1431, Aug. 2013.
- [51] M. Decker, I. Staude, M. Falkner, J. Dominguez, D. N. Neshev, I. Brener, T. Pertsch, and Y. S. Kivshar, "High-efficiency dielectric Huygens' surfaces," *Adv. Opt. Mater.*, vol. 3, no. 6, pp. 813–820, Feb. 2015.

- [52] M. Khorasaninejad, W. T. Chen, R. C. Devlin, J. Oh, A. Y. Zhu, and F. Capasso, "Metalenses at visible wavelengths: Diffraction-limited focusing and subwavelength resolution imaging," *Science*, vol. 352, no. 6290, pp. 1190–1194, Jun. 2016.
- [53] S. Wang, P. C. Wu, V.-C. Su, Y.-C. Lai, M.-K. Chen, H. Y. Kuo, B. H. Chen, Y. H. Chen, T.-T. Huang, J.-H. Wang, R.-M. Lin, C.-H. Kuan, T. Li, Z. Wang, S. Zhu, and D. P. Tsai, "A broadband achromatic metalens in the visible," *Nat. Nanotechnol.*, vol. 13, no. 3, pp. 227–232, Jan. 2018.
- [54] X. Zhang, Q. Li, F. Liu, M. Qiu, S. Sun, Q. He, and L. Zhou, "Controlling angular dispersions in optical metasurfaces," *Light: Science & Applications*, vol. 9, no. 1, May 2020.
- [55] H. Wang, Z. Zhang, B. Zhu, J. Dang, and L. Wu, "Two new approaches to optical IRSs: schemes and comparative analysis," *ArXiv*, Dec. 2020.
- [56] S. Wang, P. C. Wu, V.-C. Su, Y.-C. Lai, C. H. Chu, J.-W. Chen, S.-H. Lu, J. Chen, B. Xu, C.-H. Kuan, T. Li, S. Zhu, and D. P. Tsai, "Broadband achromatic optical metasurface devices," *Nat Commun*, vol. 8, no. 1, Aug. 2017.
- [57] K. Tekbilyk, G. K. Kurt, A. R. Ekti, A. Görçin, and H. Yanikomeroglu, "Reconfigurable intelligent surfaces empowered THz communication in LEO satellite networks," *ArXiv*, Apr. 2021.
- [58] V. K. Chapala and S. M. Zafaruddin, "Exact analysis of RIS-aided THz wireless systems over α - μ fading with pointing errors," *IEEE Commun. Lett.*, pp. 1–1, 2021.
- [59] E. N. Papatotiriou, A.-A. A. Boulogeorgos, A. Stratakou, and A. Alexiou, "Performance evaluation of reconfigurable intelligent surface assisted d-band wireless communication," in *IEEE 3rd 5G World Forum (5GWF)*. IEEE, Sep. 2020.
- [60] H. Du, J. Zhang, K. Guan, B. Ai, and T. Kürner, "Reconfigurable intelligent surface aided terahertz communications under misalignment and hardware impairments," *ArXiv*, Dec. 2020.
- [61] A.-A. A. Boulogeorgos and A. Alexiou, "Coverage analysis of reconfigurable intelligent surface assisted THz wireless systems," *IEEE Open Journal of Vehicular Technology*, vol. 2, pp. 94–110, Jan. 2021.
- [62] C. Huang, Z. Yang, G. C. Alexandropoulos, K. Xiong, L. Wei, C. Yuen, Z. Zhang, and M. Debbah, "Multi-hop RIS-empowered terahertz communications: A DRL-based hybrid beamforming design," *IEEE J. Sel. Areas Commun.*, vol. 39, no. 6, pp. 1663–1677, Jun. 2021.
- [63] Z. Wan, Z. Gao, F. Gao, M. Di Renzo, and M.-S. Alouini, "Terahertz massive MIMO with holographic reconfigurable intelligent surfaces," *IEEE Trans. Commun.*, pp. 1–1, Mar. 2021.
- [64] Y. Lu and L. Dai, "Reconfigurable intelligent surface based hybrid precoding for THz communications," *ArXiv*, Dec. 2020.
- [65] N. Abuzainab, M. Alrabeiah, A. Alkhateeb, and Y. E. Sagduyu, "Deep learning for thz drones with flying intelligent surfaces: Beam and handoff prediction," *ArXiv*, Feb. 2021.
- [66] Y. Pan, K. Wang, C. Pan, H. Zhu, and J. Wang, "UAV-assisted and intelligent reflecting surfaces-supported terahertz communications," vol. 10, no. 6, pp. 1256–1260, Jun. 2021.
- [67] —, "Self-sustainable reconfigurable intelligent surface aided simultaneous terahertz information and power transfer (stipt)," *ArXiv*, Feb. 2021.
- [68] H. Abumarshoud, L. Mohjazi, O. A. Dobre, M. Di Renzo, M. A. Imran, and H. Haas, "LiFi through reconfigurable intelligent surfaces: A new frontier for 6g?" *ArXiv*, Apr. 2021.
- [69] H. Wang, Z. Zhang, B. Zhu, J. Dang, L. Wu, L. Wang, K. Zhang, and Y. Zhang, "Performance of wireless optical communication with reconfigurable intelligent surfaces and random obstacles," *ArXiv*, Jan. 2020.
- [70] M. Najafi, B. Schmauss, and R. Schober, "Intelligent reflecting surfaces for free space optical communications," *ArXiv*, May 2020.
- [71] A. R. Ndjiongue, T. M. N. Ngatched, O. A. Dobre, A. G. Armada, and H. Haas, "Performance analysis of RIS-based nT-FSO link over G-G turbulence with pointing errors," *ArXiv*, Feb. 2021.
- [72] C. Liaskos, A. Tsioliaridou, A. Pitsillides, S. Ioannidis, and I. Akyildiz, "Using any surface to realize a new paradigm for wireless communications," *Communications of the ACM*, vol. 61, no. 11, pp. 30–33, Oct. 2018.
- [73] I. S. Gradshteyn and I. M. Ryzhik, *Table of Integrals, Series, and Products*, 6th ed. New York: Academic, 2000.
- [74] S. Z. Denic, I. Djordjevic, J. Anguita, B. Vasic, and M. A. Neifeld, "Information theoretic limits for free-space optical channels with and without memory," *Journal of Lightwave Technology*, vol. 26, no. 19, pp. 3376–3384, Oct. 2008.
- [75] F. Benkhelifa, Z. Rezki, and M. Alouini, "Low SNR capacity of FSO links over gamma-gamma atmospheric turbulence channels," *IEEE Commun. Lett.*, vol. 17, no. 6, pp. 1264–1267, Jun. 2013.
- [76] E. J. Leonardo, M. D. Yacoub, and R. A. A. de Souza, "Ratio of products of α - μ variates," *IEEE Commun. Lett.*, vol. 20, no. 5, pp. 1022–1025, May 2016.
- [77] A. P. Prudnikov, Y. A. Brychkov, and O. I. Marichev, *Integral and Series: Volume 3, More Special Functions*. CRC Press Inc., 1990.
- [78] J. Wimp, "A class of integral transforms," *Proceedings of the Edinburgh Mathematical Society*, vol. 14, no. 1, pp. 33–40, Jun. 1964.
- [79] L. Slater, *Generalized hypergeometric functions*. Cambridge: Cambridge University Press, 2008.
- [80] Y.-W. Huang, H. W. H. Lee, R. Sokhoyan, R. A. Pala, K. Thyagarajan, S. Han, D. P. Tsai, and H. A. Atwater, "Gate-tunable conducting oxide metasurfaces," *Nano Lett.*, vol. 16, no. 9, pp. 5319–5325, Aug. 2016.
- [81] B. Ratni, A. de Lustrac, G.-P. Piau, and S. N. Burokur, "Reconfigurable meta-mirror for wavefronts control: Applications to microwave antennas," *Opt. Express*, vol. 26, no. 3, p. 2613, Jan. 2018.
- [82] L. Andrews, R. L. Phillips, and C. Y. Hopen, *Laser Beam Scintillation with Applications*. SPIE Press, 2001.
- [83] G. Karagiannidis, T. Tsiftsis, and R. Mallik, "Bounds for multihop relayed communications in Nakagami-m fading," *IEEE Trans. Commun.*, vol. 54, no. 1, pp. 18–22, Jan. 2006.
- [84] A.-A. A. Boulogeorgos and A. Alexiou, "How much do hardware imperfections affect the performance of reconfigurable intelligent surface-assisted systems?" *IEEE Open Journal of the Communications Society*, vol. 1, pp. 1185–1195, 2020.
- [85] A.-A. A. Boulogeorgos, N. D. Chatzidiamentis, and G. K. Karagiannidis, "Energy detection spectrum sensing under RF imperfections," *IEEE Trans. Commun.*, vol. 64, no. 7, pp. 2754–2766, Jul. 2016.
- [86] T. Schenk, *RF Imperfections in High-Rate Wireless Systems*. The Netherlands: Springer, 2008.
- [87] A.-A. A. Boulogeorgos and G. K. Karagiannidis, "Energy detection in full-duplex systems with residual RF impairments over fading channels," *IEEE Wireless Commun. Lett.*, vol. 7, no. 2, pp. 246–249, Apr. 2018.
- [88] J. Ma, L. Moeller, and J. F. Federici, "Experimental comparison of terahertz and infrared signaling in controlled atmospheric turbulence," *J. Infrared Millim. Terahertz Waves*, vol. 36, no. 2, pp. 130–143, Nov. 2014.
- [89] M. Taherkhani, Z. G. Kashani, and R. A. Sadeghzadeh, "On the performance of THz wireless LOS links through random turbulence channels," *Nano Commun. Networks*, vol. 23, p. 100282, Feb. 2020.
- [90] ITU-R, "Attenuation by atmospheric gases," ITU-R, Tech. Rep., Sep. 2013.
- [91] R. Hill, R. Bohlander, S. Clifford, R. McMillan, J. Priestly, and W. Schoenfeld, "Turbulence-induced millimeter-wave scintillation compared with micrometeorological measurements," *IEEE Trans. Geosci. Remote Sens.*, vol. 26, no. 3, pp. 330–341, May 1988.
- [92] J. Kokkonen, J. Lehtomäki, and M. Juntti, "A line-of-sight channel model for the 100-450 gigahertz frequency band," *EURASIP Journal on Wireless Communications and Networking*, vol. 2021, no. 1, apr 2021.
- [93] J. Kokkonen, J. M. Jornt, V. Petrov, Y. Koucheryavy, and M. Juntti, "Channel modeling and performance analysis of airplane-satellite terahertz band communications," *IEEE Trans. Veh. Technol.*, vol. 70, no. 3, pp. 2047–2061, mar 2021.
- [94] A.-A. A. Boulogeorgos, E. N. Papatotiriou, and A. Alexiou, "Analytical performance assessment of THz wireless systems," *IEEE Access*, vol. 7, no. 1, pp. 1–18, Jan. 2019.
- [95] M. Taherkhani, R. A. Sadeghzadeh, and Z. G. Kashani, "Attenuation analysis of THz/IR waves under different turbulence conditions using Gamma-Gamma model," in *Iranian Conference on Electrical Engineering (ICEE)*. IEEE, May 2018.
- [96] A. W. Marshall, I. Olkin, and B. C. Arnold, *Inequalities: Theory of Majorization and Its Applications*. Springer-Verlag GmbH, 2010.
- [97] A.-A. A. Boulogeorgos, J. M. Jornt, and A. Alexiou, "Directional terahertz communication systems for 6g: Fact check: A quantitative look," *IEEE Veh. Technol. Mag.*, pp. 2–10, Oct. 2021.
- [98] D. Gunderson, *Handbook of mathematical induction : Theory and applications*. Boca Raton, FL: CRC Press, 2011.
- [99] A. M. Mathai and R. K. Saxena, "Particular cases of Meijer's G-function," in *Lecture Notes in Mathematics*. Springer Berlin Heidelberg, 1973, ch. 2, pp. 41–68.
- [100] W. R. Inc., "The Wolfram functions site," <http://functions.wolfram.com/07.34.16.0001.01>, accessed: 2021-06-08.